

ATOMISTIC STUDIES ON IRRADIATION DAMAGE IN IRON

A Thesis
Presented to
The Academic Faculty

by

Erin M. G. Hayward

In Partial Fulfillment
of the Requirements for the Degree
Master of Science in Nuclear and Radiological Engineering in the
School of Mechanical Engineering

Georgia Institute of Technology
April 2010

ATOMISTIC STUDIES ON IRRADIATION DAMAGE IN IRON

Approved by:

Professor Chaitanya Suresh Deo, Advisor
Department of Nuclear and Radiological
Engineering
Georgia Institute of Technology

Dr. Ting Zhu
Department of Mechanical Engineering
Georgia Institute of Technology

Dr. Weston Stacey
Department of Nuclear and Radiological
Engineering
Georgia Institute of Technology

Date Approved: April 2, 2010

TABLE OF CONTENTS

LIST OF TABLES	v
LIST OF FIGURES	vi
ABSTRACT	vii
I INTRODUCTION	1
1.1 Basics of Radiation Damage	1
1.2 Dislocations in Crystals	1
1.3 Motivation	3
II DAMAGE CASCADES	5
2.1 Literature Review	5
2.2 Computational Methods	6
2.2.1 Cascade Features	6
2.2.2 Counting Defects	8
2.2.3 Potentials	10
2.3 Results	12
2.3.1 Cascades in pure Fe at different energies	12
2.3.2 Cascades in pure Fe vs FeH	13
III INTERACTION OF DEFECTS WITH DISLOCATIONS	17
3.1 Literature Review	17
3.2 Linear Elastic Theory and the Dipole Tensor	18
3.2.1 Constructing the Dipole Tensor	19
3.2.2 Transformation Matrix	23
3.3 Atomistic Methods	24
3.3.1 Edge	24
3.3.2 Screw	24
3.4 Comparison of Dipole Tensor Calculations with Atomistics	25
3.4.1 Edge	25
3.4.2 Screw	31
3.5 Discussion	38

IV	CONCLUSIONS	40
APPENDIX A	MANY-BODY EAM AND FS POTENTIALS	41
REFERENCES		43

LIST OF TABLES

1	Simulation box sizes for various cascade energies	7
2	Defect data for 5 keV PKAs in pure Fe	13
3	Defect data for 10 keV PKAs in pure Fe	13
4	Defect data for 20 keV PKAs in pure Fe	14
5	Defect data for 10 keV PKAs in H-Fe, potential A	14
6	Defect data for 10 keV PKAs in H-Fe, potential B	15

LIST OF FIGURES

1	Edge and screw dislocation structures.	2
2	Comparison of PKA initial directions	8
3	Profiles of cascades in pure Fe at varying energies	9
4	The Wigner-Seitz supercell method illustrated	10
5	Four snapshots from a 10 keV cascade in pure Fe.	11
6	Percentage of surviving defects vs peak number	16
7	Schematic for generating the dipole tensor for a generic defect in a bcc lattice	20
8	Convergence of P_{ii} for a vacancy	21
9	Edge dislocation simulation cell	25
10	Edge dislocation geometry	26
11	Screw dislocation simulation cell	27
12	DTC vs atomistics for vacancies near an edge dislocation.	29
13	DTC vs atomistics for $[1 \bar{1} 0]$ dumbbells near an edge dislocation	30
14	Reorganization of a $[1 \bar{1} 0]$ dumbbell into a jog	30
15	Jogs in an edge dislocation	31
16	DTC vs atomistics for $\langle 1 1 0 \rangle$ dumbbells near an edge dislocation	32
17	Interaction energy of vacancies with screw dislocation	33
18	Color representation of interaction energies of $[1 \bar{1} 0]$ dumbbells with a screw dislocation from atomistics.	35
19	Color representation of interaction energies of $[1 \bar{1} 0]$ dumbbells with a screw dislocation from theory.	36
20	The most favorable orientations and positions for defects around a screw dislocation.	37

ABSTRACT

Two topics involving irradiation damage in α -iron have been considered. First, damage cascades representative of those that would be induced by radiation have been simulated using molecular dynamics (MD). The number and type of defects produced are compared for pure iron and iron with a small hydrogen concentration. Second, the interaction energy between point defects and line dislocations has been calculated for a number of configurations, using both molecular statics methods and calculations based on linear elastic continuum theory and the dipole force tensor. Results from both methods are compared. Results from these two topics are relevant for predicting macroscopic behaviors such as creep and plasticity in reactor structural materials.

CHAPTER I

INTRODUCTION

1.1 Basics of Radiation Damage

Radiation damage occurs when incident particles transfer some or all of their energy to atoms in a solid, resulting in a change to the original structure.

The process involves several steps. First, the incident radiation has an interaction with an atom in the crystal lattice. In a basic model, if the energy transferred in this interaction is greater than the binding energy of the lattice atom, the lattice atom will be displaced from its site. This atom is known as the primary knock-on atom (PKA). The PKA then goes on to interact with other atoms in the crystal, removing them from their sites and generating a displacement cascade. This process continues until the energy has dissipated, and all of the atoms have come to rest in the crystal. There may be atoms that come to rest in between lattice sites, creating interstitials, and leaving holes in their original sites, creating vacancies.

A typical cascade takes only picoseconds to occur. On a longer time scale, vacancies and interstitials diffuse through the material and may recombine, healing the material, or may crowd with other defects or their own kind, generating voids and clusters. More information on cascades can be found in [57, 49].

1.2 Dislocations in Crystals

A dislocation is a topological irregularity in a crystal structure, due to extra or shifted planes of atoms. There are two distinct types of dislocations, edge and screw. In real crystals, dislocations are often have characteristics of both types and are considered mixed.

Consider a perfect crystal cube. An edge dislocation occurs when an extra half-plane of atoms is inserted into the crystal, causing distortion of nearby planes. A screw dislocation could be generated by slicing the cube along a plane and displacing the atoms on one side by an amount b with respect to the other side. This creates a helical path around the

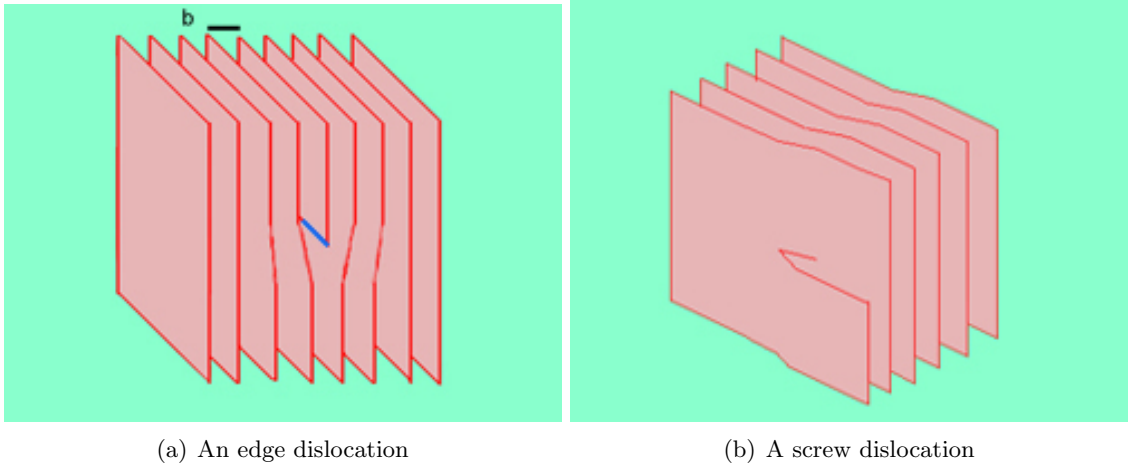


Figure 1: Basic structures for edge and screw dislocations.

dislocation (the end of the cut) line. Schematics of both types can be seen in Figure 1.

To quantify the distortion, two variables are associated with a dislocation: ξ , the dislocation line, and \mathbf{b} , the Burgers vector. The direction of ξ can arbitrarily be assigned; the direction of \mathbf{b} is defined with respect to it. Looking down the positive ξ direction, trace a clockwise circuit enclosing the dislocation core, beginning in an area of perfect crystal. The Burgers vector is defined as the vector required to close the circuit.

Dislocations have two methods of locomotion: climb and glide. Climb occurs when a dislocation emits a vacancy or interstitial. It is dependent on the rate at which defects diffuse through the material, and it is a non-conservative process. In an unirradiated environment, climb becomes important only at higher temperatures, because the equilibrium concentration of point defects is generally low. Under irradiation, defect concentrations are elevated, and climb leads to creep at lower temperatures.

Glide is not dependent on defect diffusion. It is simply the motion of the dislocation along its glide plane, and it is caused by the application of shear stress to the bulk. Glide to the surface of the crystal will result in a step. Screw dislocations can glide in any direction, since \mathbf{b} and ξ are in the same direction. Edge dislocations only have one glide plane along which they can move, so climb is a more important process.

Additional resources on the basic properties of dislocations are found in [57, 11, 38, 27].

1.3 Motivation

Damage to materials under irradiation is a problem that spans multiple time and length scales. Microstructural changes can result in dramatic macroscopic behavioral changes such as creep, plasticity, radiation-induced segregation, changes in brittle to ductile transition temperature, hardening, and cracking. Since iron is the main component in steel, an essential building material for practically any modern nuclear reactor, much is to be gained from understanding atomic scale damage events and interactions.

In this paper, the investigation of radiation damage cascades at varying energies will give an understanding of how point defects initially form under irradiation. Then, the interaction between line dislocations and irradiation induced point defects will be analyzed, providing insight into one of the most important macroscopic properties of steels, creep.

Movement of dislocations and point defects are the driving force behind creep, a macroscopic effect in which a material elongates in a particular direction over time. Creep of metals and alloys under irradiation has been the subject of many experimental and theoretical studies for more than 30 years. Although a vast amount of knowledge of irradiation creep has accumulated, the database on irradiation creep comes from many relatively small experiments, and there were often differences in experimental conditions from one study to the next. Theoretical models are based on linear elasticity. Among the many theories that exist to describe the driving force for irradiation creep, the most important are the SIPN, SIPA, and SIPA-AD effects.

Stress Induced Preferential Nucleation of loops (SIPN) [26] is based on the idea that the application of external stress will result in an increased number of dislocation loops nucleating on planes of preferred orientations. Interstitial loops will tend to be oriented perpendicular to the applied tensile stress, while vacancy loops will prefer to be oriented parallel to the stress. The net result is elongation of the solid in the direction of applied stress. While there is some experimental support of this theory, it is thought that it cannot account fully for creep seen in materials.

An alternative theory is Stress Induced Preferential Absorption/Attraction (SIPA) [24, 7, 6]. The essential idea behind SIPA is that interstitials are preferentially absorbed by

dislocations of particular orientations, resulting in climb; this is described by an elastic interaction between the stress fields of the defect and dislocation. A variant on SIPA that accounts for anisotropic diffusion is SIPA-AD. This theory uses the full diffusion equations, derived by Dederichs and Schroder [15], to take into account anisotropic stress fields. Savino and Tomé developed this theory and found that it generally gives a larger contribution to dislocation climb than the original SIPA [43]. Thorough reviews of many dislocation creep models have been prepared by Matthews and Finnis [33] and Bullough and Wood [8].

These models go a long way towards explaining irradiation creep due to dislocations; however, all models based on linear elasticity break down near a dislocation core due to $1/r$ terms in the stress and strain field expressions. Atomistic calculations do not suffer from this problem, so they can be used to verify the range of validity of theoretical expressions and successfully predict true behavior at the core.

CHAPTER II

DAMAGE CASCADES

2.1 Literature Review

The study of irradiation damage cascades has been a popular topic over the last fifteen or so years. A thorough literature review of the many different of damage cascade simulations, such as binary collision approximation and kinetic Monte Carlo, that have been performed in a variety of materials is beyond the scope of this paper. The following brief review will concentrate solely on molecular dynamics simulations in α -Fe.

The first published study was performed by Calder and Bacon in 1993 [9]. Eighty cascades with PKAs of up to 5 keV were analyzed for properties such as percent of defects surviving relaxation, channeling properties, temperature dependence, and clustering. The potential used was developed by Finnis and Sinclair [18] and stiffened by Calder and Bacon to treat small interatomic distance properly. This article established a large base of data for future papers to compare with.

Following this initial study, many papers came out which utilized both the modified FS potential mentioned above and competing multi-body potentials including those from Haftel and Andreadis [22], Johnson and Oh [29], Harrison and Voter [23], and Simonelli et al. [46]. These papers had three main motivations: to generate data from a new potential, to compare data between two or more potentials, or to compare damage in α -Fe with that in another material such as copper. The main difficulties in comparing results from different authors are defining what makes up a cluster of defects and non-reporting of exactly how cascades were generated. A thorough review of these problems, as well as a summary of results from many papers, was written by Malerba [32].

Many authors contributed to generate databases; some papers of note are described here. Stoller, Odette, and Wirth [50], using the FS potential modified by Calder and Bacon, ran a number of cascades at energies up to 40 keV. They found evidence for vacancy clustering,

a feature not seen in previous works. Bacon, Gao, and Osetsky [3] performed a study comparing the cascade characteristics of bcc, hcp, and fcc metals. They found that there were no major differences in interstitial and vacancy production, so concluded that any differences observed experimentally must be due to evolution following the primary damage event. Caturla et al. [10] compared bcc Fe with fcc Cu, finding that clustering in Fe was at least an order of magnitude less than in Cu. Terentyev et al. [51] produced a study looking solely at differences between four available potentials by applying the same defect counting criteria to each. They found that the stiffness of a potential, a somewhat arbitrary feature, was the most important factor in determining cascade properties.

A literature search did not reveal any papers with cascade results for iron infused with hydrogen, the topic of this paper. However, there are a few studies available on a similar topic, iron containing helium. Both of these elements have relevance for a fusion reactor system. Yang et al. [58] found that iron containing substitution helium atoms tends to form large vacancy clusters, while only a few small ones are seen in pure Fe. Additional papers from Yu et al. [59] and Schaublin and Baluc [44] confirm this finding and conclude that the presence of He does not make a difference in the number of defects initially created.

2.2 Computational Methods

2.2.1 Cascade Features

All cascade simulations were performed using the LAMMPS molecular dynamics code [40]. Cascade energies of interest ranged from 5 keV to 20 keV, although some diagnostics and checks were run with lower energy cascades.

Periodic boundary conditions were used, so care was taken to ensure the simulation boxes were large enough to avoid image effects. Cascades were visually inspected to check for self-interference; in addition, test runs were performed with larger boxes to make sure the number of defects seen was representative of a cascade in an infinite medium. Table 1 shows the dimensions of the simulation box for the various energies.

For the pure iron cascades, the simulation box was filled with perfect bcc lattice. For the hydrogen cascades, an appropriate number of tetrahedral interstitial sites [28] were

Table 1: Simulation box sizes for various cascade energies. The second column indicates lattice spacings in each direction, creating a cubic simulation box.

Cascade Energy (keV)	Lattice Spacings (a_0)	Number of Fe Atoms
≤ 3	30	54,000
5	50	250,000
10	60	432,000
20	100	2,000,000

randomly selected to hold H atoms; every regular bcc site still contained an iron atom.

At the beginning of each simulation, equilibration of the lattice was performed at 300 K for 10 ps. A damped Nose-Hoover thermostat was used with a NVT ensemble, in which the number of atoms, volume of the box, and the temperature are kept constant.

For pure iron, a relatively large timestep of 10 fs was used for this stage of the simulation since atoms would not be moving very far. The FeH systems were more sensitive, so a timestep of 1 fs was used. Additionally, before equilibration the FeH systems were minimized with conjugate gradient methods to allow the atoms nearest to the H interstitials to relax.

To simulate damage from a neutron hitting the bulk, a random atom near the center of the simulation box is chosen to be the primary knock-on atom. This atom is given a velocity corresponding to the desired cascade energy, and the simulation is continued.

Cascades were induced in the $\langle 1\ 3\ 5 \rangle$ direction. This direction is often used in the literature to be representative of a random direction; it also has the benefit that it reduces channeling. 1 keV simulations were performed this direction in pure Fe, as well as in the $\langle 1\ 0\ 0 \rangle$, $\langle 1\ 1\ 0 \rangle$, and $\langle 1\ 1\ 1 \rangle$ directions to verify this claim. Six cascades were run in each direction, in a box which had been equilibrated at 100 K. The results of this test can be seen in Figure 2, with the horizontal bar indicating the average number of Frenkel pairs for each direction and the vertical error bar showing the standard deviation. Indeed, the $\langle 1\ 3\ 5 \rangle$ direction seems like a good choice to be representative of a random direction.

During this phase a microcanonical ensemble (NVE) was used, in which the number of atoms, volume of the box, and total energy are conserved. No further attempt was made to keep the box at 300 K.

A timestep of 0.1 fs was used to ensure that all the physics was captured when the atoms

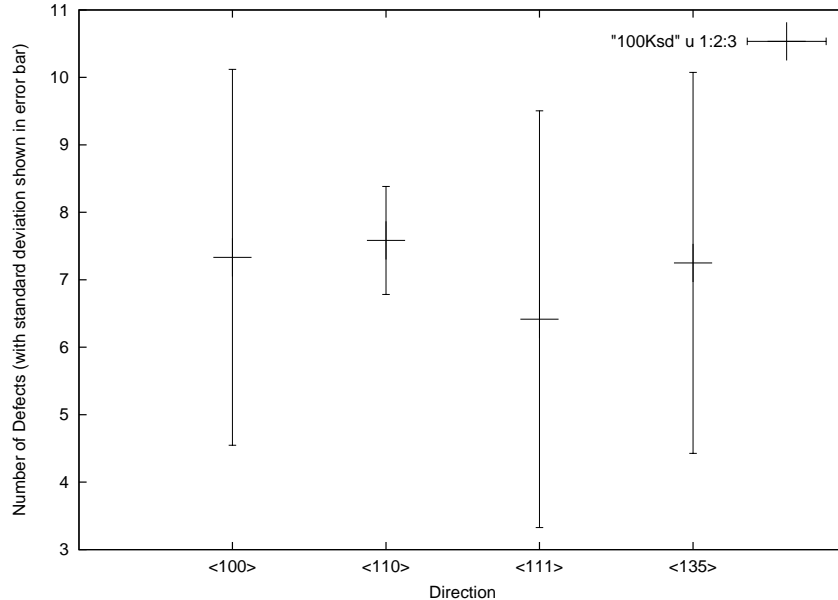


Figure 2: Comparison of PKA initial directions for 1 keV cascades. The horizontal lines show the average number of Frenkel pairs while the error bars show the standard deviation.

had close approaches. This thermal spike phase was simulated for 5 ps.

By 5 ps after the cascade is induced, the crystal has begun to anneal significantly through recombination of defects, so the timestep is adjusted to 1.0 fs for computational efficiency. For the 5 keV cascades, relaxation is performed for 5 more ps; for the 10 and 20 keV cascades, relaxation continues for 20 ps, although the atoms are fully relaxed before the end of this time. Typical cascade profiles can be seen in Figure 3.

2.2.2 Counting Defects

A post-processing tool, utilizing the well-known Wigner-Seitz supercell method, was written for counting the number of Frenkel pairs at different stages in the cascade. This method is a popular one because the entire simulation box is covered; methods that count based on distance from lattice sites may miss areas of the box. Only iron defects were counted, since all the hydrogen atoms were set up as interstitials.

First, the simulation box is broken up into cubic supercells, corresponding in size and

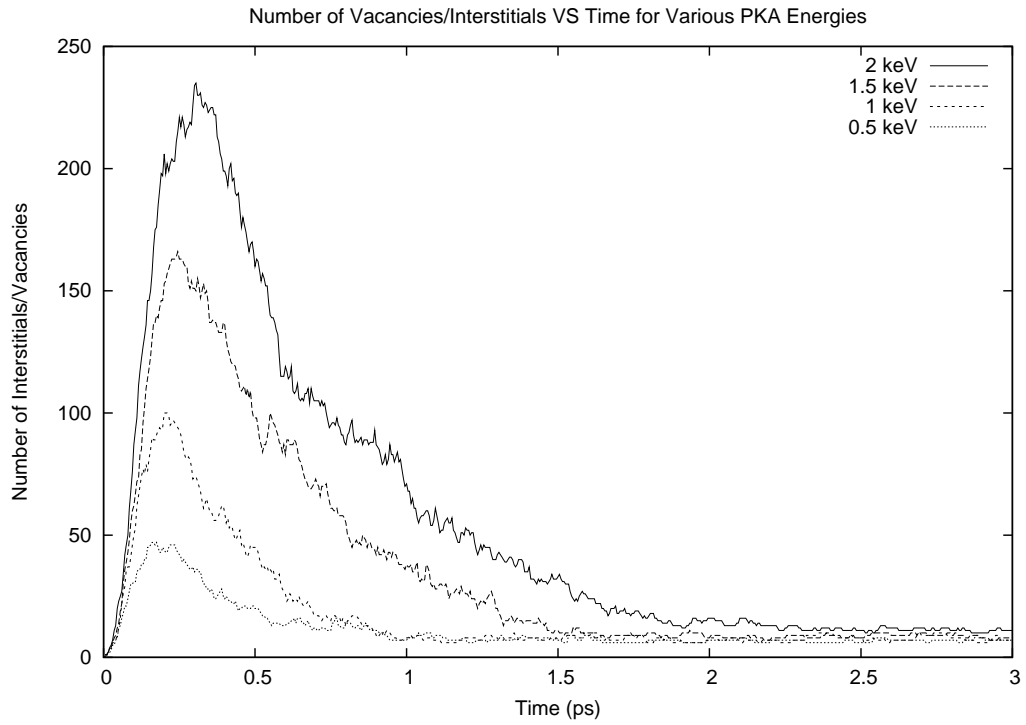


Figure 3: Profiles of cascades in pure Fe at varying energies. All cascades shown were run in cells of 54 000 atoms. An initially defect free cell quickly attains its peak number of defects during thermal spike, then the majority of defects recombine over a few ps. Cascades with more energetic PKAs peak later and take longer to relax.

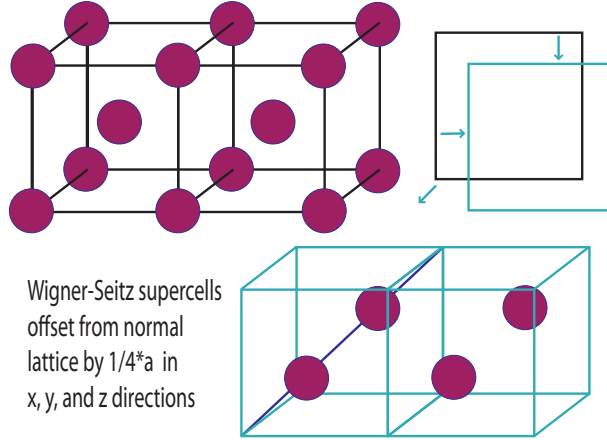


Figure 4: An illustration of the Wigner-Seitz supercell method. Supercells are constructed to be the same size as traditional bcc cells, with 2 atoms per cell in a perfect lattice. However, they are offset to eliminate counting errors due to movement about the lattice sites.

shape to, but offset from the unit lattice cubes by $\frac{1}{4}a_0$ in the x, y, and z directions. This offsetting is necessary to avoid miscounting of defects as the atoms oscillate around their lattice sites due to thermal motion. A schematic can be seen in Figure 4.

At $t = 0$, the supercells record how many iron atoms are within their bounds; this is 2 for a perfect bcc lattice. During the cascade simulation, atoms positions are recorded every n timesteps. For each of these timesteps, the supercells again calculate the number of iron atoms within their bounds and compare this number to the number at initialization. A cell is identified as having vacancies, if there are less than 2 atoms in the cell, or interstitials, if there are more than 2 atoms in the cell.

All iron atoms in any cell identified as having vacancies or interstitials are then correspondingly plotted to create animations of the cascades. In the setups with hydrogen, all hydrogen atoms were also plotted at every timestep. Snapshots from a representative cascade can be seen in Figure 5 for pure iron.

2.2.3 Potentials

Three different many-body potentials were used for the simulations. More technical information about this class of potentials, and specifically the potentials mentioned below, can be found in Appendix A.

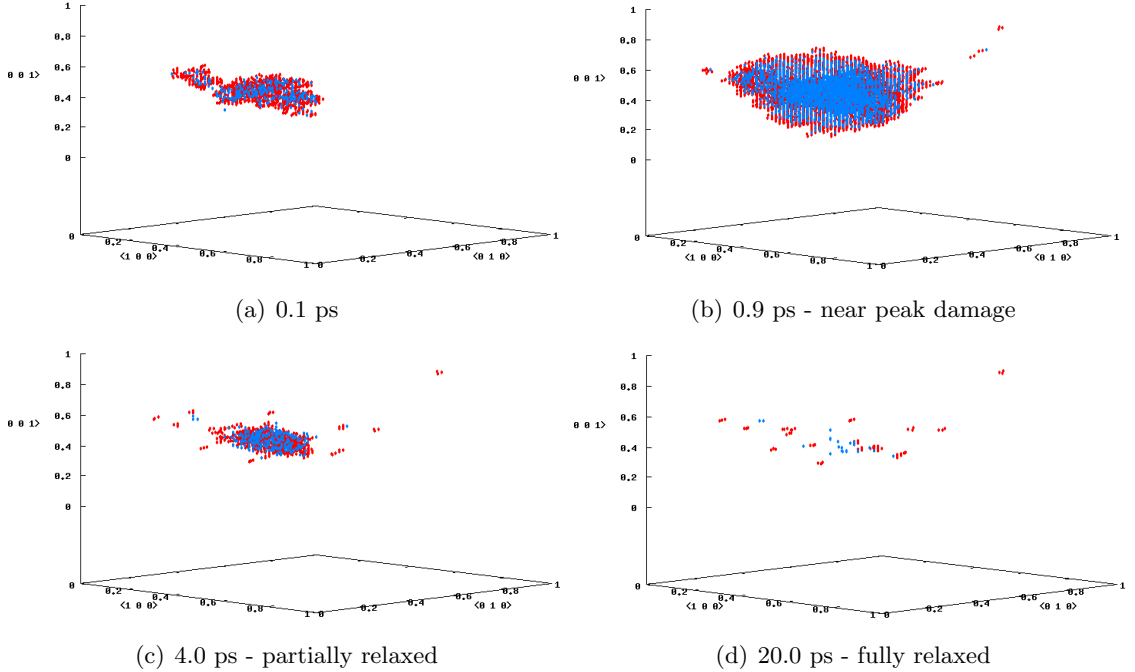


Figure 5: Four snapshots from a 10 keV cascade in pure Fe. Red dots show interstitials, blue dots show vacancies. All coordinates are scaled from 0 to 1; real box size is 171.31 Å in each dimension. Times indicated are from a reset $t = 0$ after equilibration. Note the vacancy rich core surrounded by interstitials.

For the pure Fe cascades, the embedded atom method (EAM) potential #2 from Mendeleev et al.[35] was used. This potential was generated by fitting to first-principles forces seen in the liquid state in addition to bulk crystal data and crystal defect information. Using data from a liquid-like state lets this potential give a better description of interaction at small separations than had been seen in previous iron potentials, due to the fact that atoms in liquid iron will often find themselves closer together than atoms in a solid; this is also the situation with interstitials in iron. As evidence of the effectiveness of this fitting method, this potential predicts the formation energies of interstitial dumbbells very accurately (within 3%), despite not having been fit to these parameters directly. By comparison, a potential generated by Ackland et al. [1] that was fit to all the same parameters except the liquid state overestimates these energies by up to 40% in some directions.

Two FeH potentials, which were developed by Ramasubramaniam et al.[41], were used for comparison. The first, hereafter referred to as potential A, takes the Fe-Fe interactions from potential #4 of the above mentioned Mendeleev work. This iron potential is similar to

#2, however it is fit to experimental liquid structure data instead of first-principles calculations of liquid states. The two potentials give very close results for a number of physical properties, including lattice parameter, elastic constants, and vacancy formation energy. One difference worth noting is that potential #4 predicts interstitial dumbbell formation energies 9-13% lower than does potential #2. However, the ordering of the directionality of the dumbbells is consistent; both potentials predict dumbbells in the $\langle 1\ 1\ 0 \rangle$ direction to have the lowest formation energy, followed by the $\langle 1\ 1\ 1 \rangle$ and $\langle 1\ 0\ 0 \rangle$ directions.

The second FeH potential, referred to as potential B, gets its Fe-Fe interactions from a 2004 potential from Ackland et al.[2]. This potential is simply a slightly improved version of Mendeleev et al.'s potential #2, fitted to eliminate negative thermal expansion.

To fit the Fe-H and H-H interactions, Ramasubramaniam et al. used a variant of the EAM and Finnis-Sinclair (FS) formalisms to describe the total energy of the system. Using this general many-body form, the two-body interactions ϕ and electron densities ρ are specified independently for each type of interaction. Data from first-principles DFT was used for fitting. Specifically, dissolution and binding energies for various configurations in the bulk and in the presence of vacancies were considered. A battery of tests were run to assess the performance of the potentials for a variety of situations and results were in good agreement with DFT predictions. It should be noted that two additional potentials were developed by Ramasubramaniam et al. by additionally fitting to surface data, but these potentials have inferior performance in the bulk, so they are not considered in this study.

2.3 Results

2.3.1 Cascades in pure Fe at different energies

Cascades were induced with 5, 10, and 20 keV PKAs in pure Fe. As would be expected, cascades with less energy peaked earlier and had fewer overall defects. The energy of the cascade does not greatly influence the percentage of defects surviving. For each energy, the average percentage of surviving defects was between one and two percent, with individual cascades ranging between 0.43 and 2.12 percent surviving. Data for these energies is found in Tables 2, 3, and 4.

Table 2: Data on defects from 5 keV cascades in pure Fe. N is number of Frenkel pairs, t is time in timesteps.

Case	N_{peak}	t_{peak}	$N_{surviving}$	% Surviving
1	1013	5800	16.12	1.59
2	1096	6500	5.82	0.53
3	1018	5600	13.50	1.33
4	966	5700	20.43	2.11
5	1049	5700	8.69	0.82
avg	1028.4		12.91	1.27

Table 3: Data on defects from 10 keV cascades in pure Fe. N is number of Frenkel pairs, t is time in timesteps.

Case	N_{peak}	t_{peak}	$N_{surviving}$	% Surviving
1	2569	8600	42.95	1.67
2	2993	9000	21.60	0.72
3	1960	5700	41.50	2.12
4	2890	8900	28.85	1.00
5	2990	8900	15.20	0.51
6	1966	6300	37.65	1.92
7	3082	9000	18.10	0.59
8	2957	9200	12.70	0.43
9	2620	8700	21.35	0.81
10	2948	8800	22.45	0.76
avg	2697.5		26.24	1.05

As a PKA is given more energy, the structure of the cascades changes, but the inherent recombination properties do not. That is, a cascade will tend to branch out as more energy is given to the PKA so that it takes up a larger area, but defects created will still recombine at the same rate. For example, a 5 keV cascade can be thought of as an offshoot branch of a larger 20 keV cascade.

2.3.2 Cascades in pure Fe vs FeH

To compare pure iron to iron containing hydrogen, additional cascades were performed with 10 keV iron PKAs. This energy was chosen because the size of the simulation box allows for reasonably fast computations, but there are still enough atoms to get good statistics with low solubility.

The solubility of hydrogen in iron is 0.01 at.% at 1000 K [42, 5], and significantly lower at room temperature. Even though these simulations were run at only 300 K, the above

Table 4: Data on defects from 20 keV cascades in pure Fe. N is number of Frenkel pairs, t is time in timesteps.

Case	N_{peak}	t_{peak}	$N_{surviving}$	% Surviving
1	4851	11200	40.62	0.84
2	6603	11800	71.57	1.08
3	6915	11500	68.13	0.98
4	3968	8300	80.29	2.02
5	6500	11100	53.24	0.82
6	5126	9100	50.44	0.98
avg	5660.5		60.72	1.62

Table 5: Data on defects from 10 keV cascades in Fe with 0.01 at.% H, with potential A. N is number of Frenkel pairs, t is time in timesteps.

Case	N_{peak}	t_{peak}	$N_{surviving}$	% Surviving
2	2012	7400	24.58	1.22
3	2295	7600	29.10	1.27
4	2027	7600	15.42	0.76
5	2784	8400	10.46	0.38
6	1596	6000	22.66	1.42
7	2101	6600	21.44	1.02
8	3009	8400	33.22	1.10
9	3261	8200	22.60	0.69
10	2244	7100	9.38	0.42
avg	2369.9		20.98	0.92

mentioned solubility was used with the assumption that in a fusion environment, more hydrogen may be implanted than would normally be soluble. Runs were performed with both potentials A and B to check for discrepancies.

Raw data for these simulations can be seen in Tables 3, 5, and 6. The number of surviving defects is taken as an average over the end of the simulation. At this point, the crystal is relaxed and the number of defects is fairly constant, but fluctuates slightly due to the counting method.

The simulation boxes containing hydrogen do not show markedly different results from those without. The average number of Frenkel pairs at peak time in systems with hydrogen was 2463.1, with a standard deviation of 613.8. The data from both potentials A and B was lumped to generate this figure. For pure iron, the average was 2697.5, with a standard deviation of 420.2. Even though slightly more defects are initially created in a pure iron system, the number remaining after relaxation is no greater than in systems with hydrogen.

Table 6: Data on defects from 10 keV cascades in Fe with 0.01 at.% H, with potential B. N is number of Frenkel pairs, t is time in timesteps.

Case	N_{peak}	t_{peak}	$N_{surviving}$	% Surviving
2	1328	5500	32.72	2.46
3	2766	7600	31.54	1.14
4	2829	8800	21.76	0.77
5	2697	8000	24.76	0.92
6	3398	8300	10.00	0.29
7	3307	8500	15.12	0.46
8	2176	8100	30.56	1.40
9	2839	8800	39.84	1.40
10	1666	5500	44.72	2.68
avg	2556.2		27.89	1.28

Comparing potentials involving hydrogen, the use of potential A generally results in a simulation with fewer defects compared to potential B, at both peak and final times. Also, a smaller percentage of the defects created survive. Overall, potential A gives a slightly smaller percent defects remaining number than does pure Fe, while potential B predicts a larger percentage. It is difficult to determine which trend is correct because experiments on this timescale and lengthscale are extremely hard to conduct.

A negative correlation between the percentage of surviving defects and the number of defects created at peak time is observed (see Figure 6). This trend is particularly obvious for pure iron and FeH systems with potential B and can be understood in the following way. Generally, systems with a larger number of peak defects also exhibit less branching structure, with the energy being spread out to more atoms within a smaller area. Thus in this type of system, the probability of a vacancy being near an interstitial is enhanced during relaxation, and the chances of recombination are greater.

It should be noted that the longterm behavior of iron systems containing hydrogen may be markedly different than that of pure iron systems. Hydrogen atoms diffuse through the bulk at a higher rate than self interstitials and vacancies and are likely to cluster together on the timescale of nanoseconds. These may be initiation sites for voids or interstitial clusters, resulting in different macroscopic properties than those seen in pure iron. This is an active area of research, however more thorough analysis of this topic is beyond the scope of this paper.

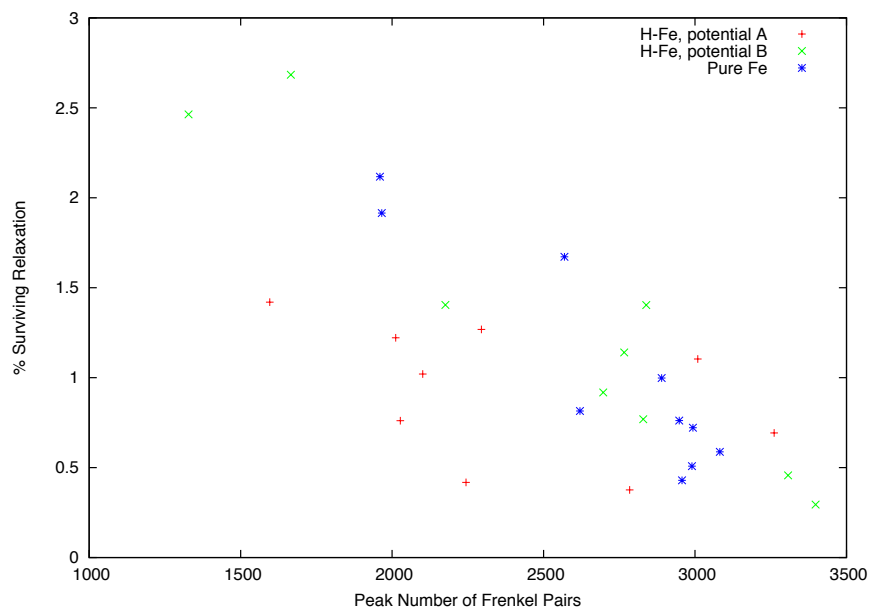


Figure 6: The percentage of defects that survive relaxation vs the peak number of defects in a system, in which a negative correlation is seen.

CHAPTER III

INTERACTION OF DEFECTS WITH DISLOCATIONS

3.1 Literature Review

Computer modeling of dislocations has a long history, beginning in the late 1960s with Vitek and Duesbery [17, 54, 55, 56]. Since then, many authors have studied how edge and screw dislocations move through material, interact with point defects, and influence macroscopic behavior.

One important quantity that has been studied is the interaction energy. The interaction energy between a point defect and a line dislocation is a measure of the favorability of the positioning of the defect with respect to the dislocation, and it is also a predictor of how the dislocation and defect may eventually combine to result in climb behavior. A negative interaction energy indicates that the defect is in a favorable position; that is, placing a defect at this particular position in the crystal lowers the system's total energy.

A theoretical model to calculate interaction energy based on the dipole tensor (discussed in more detail in the next section) was developed by Meissner et al. [34] in an anisotropic medium. This model was the basis for work by Tomé et al. [53] in which interaction energy in hexagonal close packed materials was studied near edge and screw dislocations. Both of these papers used lattice Green's functions to calculate the dipole tensors. Further works invoking this theoretical framework and the model of diffusion of point defects of Dederichs and Schoeder [15] include those of Tomé et al. [52], Monti et al. [36], and Smetniansky-de Grande et al. [21].

Also based on Meissner's theoretical formulation, a study of the migration of point defects towards line dislocations in bcc Fe was conducted by Sivak et al. [47]. This paper presents values of the dipole tensor that differ from the ones presented below. This is attributed to the fact that basic pair potential is used, which may give less accurate results than those from an EAM potential. Shastry and de la Rubia [45] looked at the interaction

between point defects and edge dislocations. Their results qualitatively agree with the ones presented in this chapter, but take far fewer cases into consideration.

Osetsky et al. [39] compare results from isotropic elasticity theory to atomistics, as applied to edge dislocation interactions with large self-interstitial clusters in iron and copper. They conclude that theory is not sufficient to explain the behavior of these systems at small distances from the core. There is also a large body of literature existing that describes the interactions between glissile line dislocations and point defects or large self-interstitial clusters. These papers do not directly calculate the interaction energy, but concentrate on the different types of structures that may be formed when various types of defects run into each other. Liu and Biner performed one such study for screw dislocations and self-interstitial clusters [31], finding two main mechanisms of transformation. Fujita et al. [20] and Bacon et al. [4] performed similar studies for edge dislocations and screw dislocations, respectively. It is beyond the scope of this paper to review all existing literature on computer simulations of dislocations. A recent review was conducted by Moriarty et al. [37].

In this chapter, the interaction energy will be calculated in two different ways and then compared. The first method involves linear elastic continuum theory and the dipole force tensor. The second method involves atomistic calculations using molecular statics.

3.2 Linear Elastic Theory and the Dipole Tensor

According to continuum theory, the interaction energy between the point defect and a dislocation a distance \mathbf{r} from each other is given by

$$E(\mathbf{r}) = -\varepsilon_{ij}(\mathbf{r})P_{ij} \quad (1)$$

where ε is the strain field of the dislocation [34] and \mathbf{P} is the dipole tensor, described in the next section. The interaction energy is defined by setting $E = 0$ at the point where the defect is far enough away from the dislocation to feel no influence; in other words, the defect sees essentially bulk material. So, defects of different configurations may be shifted by different amounts. For example, the total energy of a system with a $\langle 1\ 1\ 0 \rangle$ dumbbell will be lower than for a system with a $\langle 1\ 1\ 1 \rangle$ dumbbell.

For an edge dislocation, the non-zero components of the strain tensor in an isotropic medium [38] are given by

$$\begin{aligned}
\varepsilon_{xx} &= -\frac{b}{4\pi(1-\nu)r} \sin\theta \cos 2\theta - \frac{b}{2\pi r} \sin\theta \\
\varepsilon_{yy} &= \frac{b}{4\pi(1-\nu)r} \sin\theta(2\cos^2\theta + 1) - \frac{b}{2\pi r} \sin\theta \\
\varepsilon_{xy} &= \frac{b}{4\pi(1-\nu)r} \cos\theta \cos 2\theta
\end{aligned} \tag{2}$$

where b is the magnitude of the Burgers vector and ν is Poisson's ratio. Also, $\varepsilon_{yx} = \varepsilon_{xy}$ to give a symmetric tensor. The dislocation line $\boldsymbol{\xi}$ is defined to be in the z direction, with a Burgers vector in the x direction.

For a screw dislocation, the non-zero components are

$$\begin{aligned}
\varepsilon_{xz} &= -\frac{b}{4\pi r} \sin\theta \\
\varepsilon_{yz} &= \frac{b}{4\pi r} \cos\theta.
\end{aligned} \tag{3}$$

Again, the tensor is symmetric. The dislocation line is again in the z direction, with a parallel Burgers vector.

3.2.1 Constructing the Dipole Tensor

The influence that a point defect, either a vacancy or interstitial, has on its neighbors can be characterized by the dipole tensor \mathbf{P} . Components are calculated by

$$P_{ij} = \sum_{k=1}^N [S_i^{(k)} + d_i^{(k)}] F_j^{(k)}$$

where the sum is over N neighbors of the defect, \mathbf{S} denotes the perfect lattice position of a neighbor with respect to the defect, \mathbf{d} is the displacement from the perfect lattice position caused by the defect's presence, and \mathbf{F} is the Kanzaki force [30]. Kanzaki forces are defined as the forces on neighbors of the defect that must be applied to maintain the displaced structure when the defect is removed, or the portion of the total force on a neighbor due to the defect when in a relaxed position.

To find these forces and displacements, atomistic simulations were performed in which a defect was introduced into a perfect lattice. Conjugate gradient minimization was performed

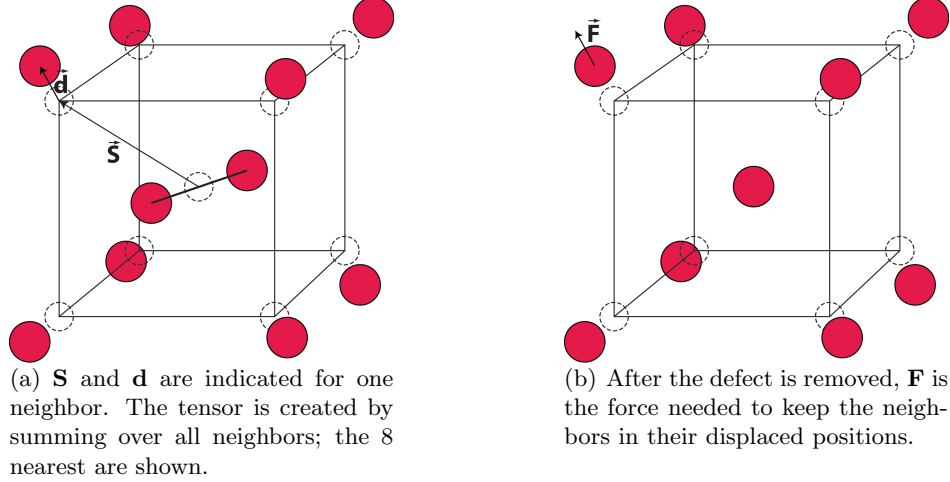


Figure 7: Schematic for generating the dipole tensor for a generic defect in a bcc lattice. Dotted circles denote perfect lattice positions. Red circles denote displaced atom positions caused by the presence of the defect.

to relax the lattice. Care must be taken that the lattice is fully relaxed; this was checked by ensuring that no component of force on any atom was larger than 1×10^{-15} eV/Å. Then, the defect was removed and the lattice restored to its original state, but with the neighbors maintaining their displacements. The force produced by the defect site on the neighbors can then be measured; it is equal in magnitude but opposite in sign to the force produced by the defect itself. A schematic of the process can be seen in Figure 7. The multi-body potential used to find the values of \mathbf{S} , \mathbf{d} , and \mathbf{F} is from Ackland et al [2].; this is the same potential which provides the Fe part of potential B referred to in the previous chapter. Advantages of this potential for dislocation calculations are discussed in the next section.

It is clear that the number of neighbors taken into consideration can influence the values of the components of \mathbf{P} . Convergence testing was done by considering successive neighbor shells in the calculation. A cube of iron, $20a_0$ in each dimension, was modeled, with the simulation box divided into two regions. A smaller cube of dimensions $17a_0$ was centered in the larger box, and surrounded by atoms frozen in their perfect sites to simulate pure bulk material. Periodic boundary conditions were applied, however the box size was large enough to eliminate any artifacts from Images of the defect. All calculations of \mathbf{P} were done in the crystal coordinate system ($\mathbf{x} = [1\ 0\ 0]$, $\mathbf{y} = [0\ 1\ 0]$, $\mathbf{z} = [0\ 0\ 1]$).

For a vacancy in an isotropic medium such as bcc iron, \mathbf{P} will be a symmetric diagonal

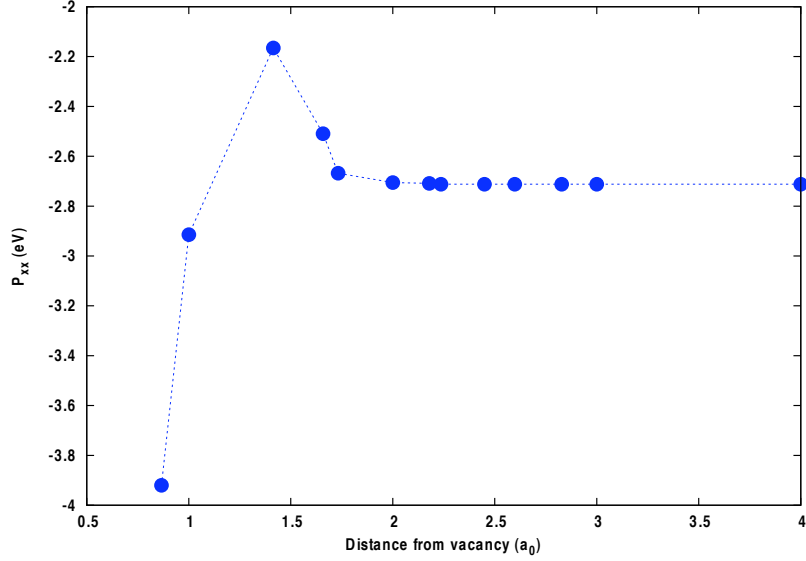


Figure 8: P_{ii} calculated considering different neighbor shells for a vacancy in bcc iron. Points denote neighbor shells. Convergence to -2.71185 eV is reached after considering 9 neighbor shells.

matrix, with $P_{xx} = P_{yy} = P_{zz}$ and all other components equal to zero. It was found that for this potential in bcc iron, $\text{Tr}(\mathbf{P}) = -8.13555$ eV, or $P_{ii} = -2.71185$ eV in the crystal coordinate system. This value is reached when 9 or more neighbor shells, or atoms up to $2.4495a_0$ away, are considered. A graph of P_{ii} considering different numbers of neighbor shells can be seen in Figure 8. The full matrix is

$$\mathbf{P}(\text{vacancy}) = \begin{pmatrix} -2.71185 & 0 & 0 \\ 0 & -2.71185 & 0 \\ 0 & 0 & -2.71185 \end{pmatrix} \text{ eV} \quad (4)$$

The dipole tensor can also be calculated for the saddle point of a vacancy undergoing diffusion. A vacancy trading places with one of its nearest neighbors is the most likely case; this is a movement in a $\langle 1 \ 1 \ 1 \rangle$ direction. To find the saddle point configuration, temperature accelerated dynamics (TAD) [48] was used to detect the transition of a system with one vacancy in it. The nudged elastic band method [25] was employed to measure where along the path a saddle point was located, and the forces and displacements were

calculated as before. It was found that there is a local minimum halfway between the two regular lattice positions, with symmetric saddle points on either side. The vacancy must overcome a barrier of 0.6395 eV to reach this intermediate minimum, at 0.5488 eV above the reference state. Moving in the $\langle 1 1 1 \rangle$ direction, the tensor for the intermediate local minimum is

$$\mathbf{P}(\text{vacancy}^{lm}) = \begin{pmatrix} -4.242 & -1.467 & -1.467 \\ -1.467 & -4.242 & -1.467 \\ -1.467 & -1.467 & -4.242 \end{pmatrix} \text{ eV.} \quad (5)$$

and the tensor for the saddle point is

$$\mathbf{P}(\text{vacancy}^{sp}) = \begin{pmatrix} -5.43 & -2.59 & -2.59 \\ -2.59 & -5.43 & -2.59 \\ -2.59 & -2.59 & -5.43 \end{pmatrix} \text{ eV.} \quad (6)$$

Vacancy hops in other directions are much less likely to occur. Nudged elastic band calculations predict a barrier of 2.63 eV for $\langle 1 0 0 \rangle$ hops and 4.91 eV for $\langle 1 1 0 \rangle$ hops.

For interstitial dumbbells, anisotropy exists in the dipole tensor and the off diagonal components may be non-zero in the crystal coordinate system. The dipole tensors, calculated with 2890 neighbors, for the three interstitial dumbbell configurations in bcc iron are given below:

$$\mathbf{P}([1 1 0]) = \begin{pmatrix} 10.2056 & 4.7428 & 0 \\ 4.7428 & 10.2056 & 0 \\ 0 & 0 & 10.9080 \end{pmatrix} \text{ eV} \quad (7)$$

$$\mathbf{P}([1 0 0]) = \begin{pmatrix} 8.7977 & -1.0332 & -1.0332 \\ -1.0332 & 8.1689 & 2.9766 \\ -1.0332 & 2.9766 & 8.1689 \end{pmatrix} \text{ eV} \quad (8)$$

$$\mathbf{P}([1 1 1]) = \begin{pmatrix} 8.5493 & 4.6977 & 4.6977 \\ 4.6977 & 8.5493 & 4.6977 \\ 4.6977 & 4.6977 & 8.5493 \end{pmatrix} \text{ eV} \quad (9)$$

It should be noted that the $\langle 1 1 1 \rangle$ dumbbell is rather unstable. With thorough minimization, it consistently reconfigured into some variant of a $\langle 1 1 0 \rangle$ dumbbell. When

calculating this \mathbf{P} , minimization was allowed to run long enough to allow the $\langle 1\ 1\ 1 \rangle$ dumbbell to come to its equilibrium distance, then the dumbbell atoms were frozen for further minimization. In this case, no component of force was allowed to be larger than 1×10^{-9} eV/Å.

The tensor is sensitive to the direction in which a vacancy is moving or a dumbbell is lying. Tensors can easily be generated for alternative directions following two simple rules:

1. Permutations of direction vector components result in the switching of appropriate rows and columns of the tensor.
2. Any sign change in a particular component of the direction vector will result in a sign change of the off-diagonal elements of the tensor that correspond to that component.

For example, the dipole tensor for a $[1\ 0\ \bar{1}]$ dumbbell would be:

$$\mathbf{P}([1\ 0\ \bar{1}]) = \begin{pmatrix} 10.2056 & 0 & -4.7428 \\ 0 & 10.9080 & 0 \\ -4.7428 & 0 & 10.2056 \end{pmatrix} \text{ eV}$$

3.2.2 Transformation Matrix

Before the interaction energy can be calculated, the dislocation strain field and the dipole tensor must be described in the same coordinate system. The crystal coordinate system is the most intuitive, and the strain tensor is easily described into this system via a transformation matrix:

$$\boldsymbol{\epsilon}^C = \mathbf{T}\boldsymbol{\epsilon}^D\mathbf{T}^\dagger \quad (10)$$

where \mathbf{T} has the normalized box vectors of the dislocation coordinate system as its columns, and \mathbf{T}^\dagger is the transpose of \mathbf{T} . The coordinate systems used to describe the dislocations are described in the next section.

Individual direction vectors can be translated between coordinate systems in a similar way:

$$\mathbf{v}^C = \mathbf{T}\mathbf{v}^D.$$

3.3 Atomistic Methods

Dislocations were introduced into bulk iron following linear elastic displacement theory. Periodic boundary conditions are used in the direction of the dislocation line; the other two boundaries are frozen some distance from the core to preserve the linear elastic field. Following initial displacement by theory, the atoms near the core are allowed to relax under conjugate gradient minimization to correctly find the core configuration, while atoms on the boundaries are frozen to preserve the linear elastic field. Details for particular types of dislocations are given below.

The potential used for both the above dipole tensor calculations and the following atomistic calculations is from Ackland et al [2].; this is the same potential which provides the Fe part of potential B referred to in the previous chapter. This potential is one of the few available multi-body potentials to predict the non-degenerate compact core structure of a screw dislocation in bcc iron [16], as seen in Frederiksen and Jacobsen’s *ab initio* calculations [19].

Vacancies and interstitials were introduced into the fully relaxed configurations, then minimized again with conjugate gradient methods before measuring the energy of the system. Both LAMMPS [40] and Art Voter’s clsmn codes were used for minimization and analysis. In the following sections, all atomistics were performed at 0 K.

3.3.1 Edge

Edge dislocations were created with Burgers vector $\mathbf{b} = \frac{1}{2} [1\ 1\ 1]$ and the dislocation line $\boldsymbol{\xi}$ in the $[1\ 1\ \bar{2}]$ direction. Box vectors are given by $[1\ 1\ 1]$, $[1\ \bar{1}\ 0]$, and $[1\ 1\ \bar{2}]$, respectively x , y , and z . A system of 118,244 atoms was used, 61,368 of which are allowed to move. The full setup can be seen in Figure 9. A zoomed in view of the core can be seen in Figure 10(a).

3.3.2 Screw

Screw dislocations were created in the coordinate system with box vectors $[1\ \bar{1}\ 0]$, $[\bar{1}\ \bar{1}\ 2]$, and $[1\ 1\ 1]$. The Burgers vector has magnitude $\sqrt{3}a_0/2$ in the $[1\ 1\ 1]$ direction; the dislocation line is parallel. A system of 100,095 atoms was used, 64,005 of which are allowed to move.

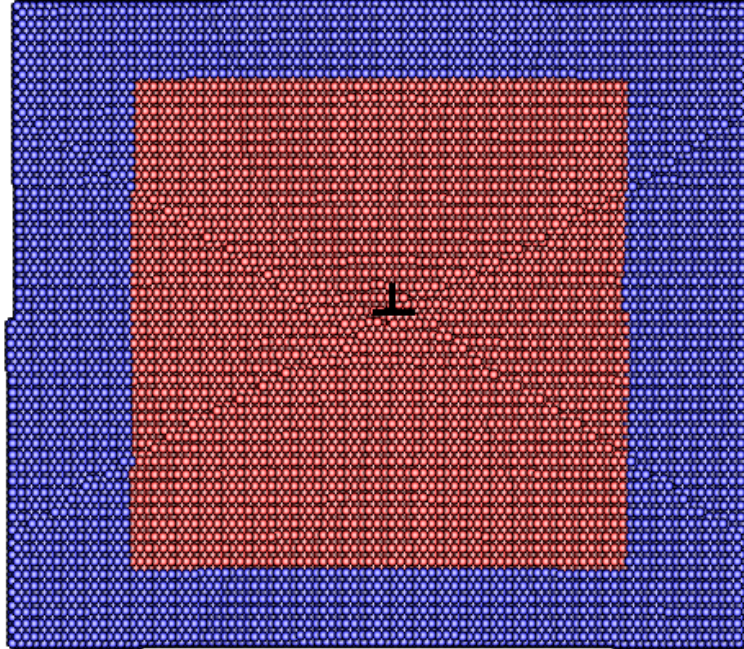


Figure 9: The edge dislocation. Frozen atoms are in blue, free are red. The simulation box is about 206 Å wide, 207 Å tall, and 27.98 Å deep in the periodic direction.

The setup can be seen in Figure 11.

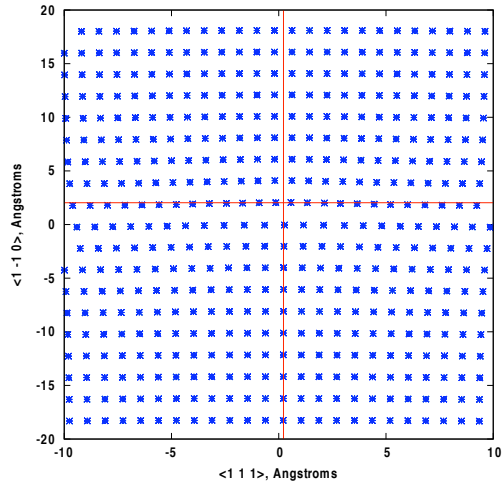
3.4 Comparison of Dipole Tensor Calculations with Atomistics

It is extremely valuable to be able to compare atomistic simulations with calculations utilizing Equation 1 (referred to in this paper as dipole tensor calculations, or DTC) for interaction energy between defects and dislocations. Continuum theory is known to break down very close to the core, where equations predict singularities, but atomistics provides a reliable way to gain information in these regions. The distance from the core at which DTC becomes reliable can also be judged from comparison.

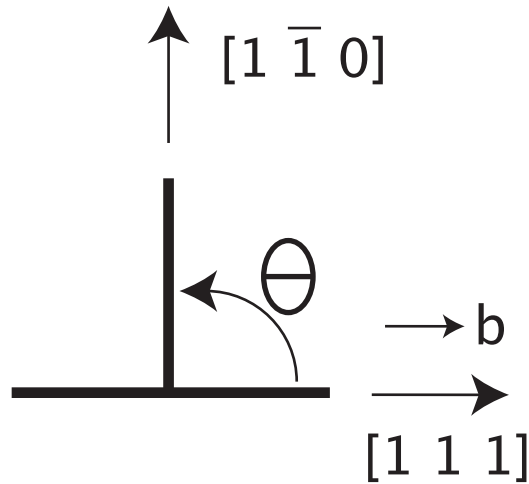
3.4.1 Edge

3.4.1.1 Vacancy

To create the graph shown in Figure 12(a), in turn each atom in the system is removed, the system is minimized, and the energy is measured. Although DTC and atomistics agree quite well far from the core (Figure 12(c)), close to the core there is much disagreement. For vacancies placed in the tensile region, below the half plane, DTC predicts that the

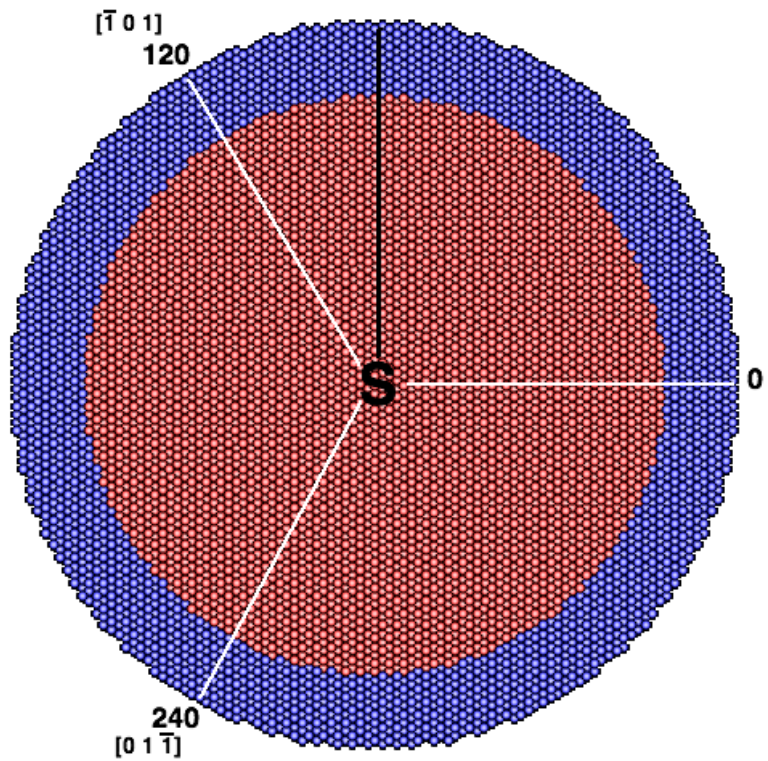


(a) Close up view of the core of the edge dislocation. Cross hairs denote where the core is defined. The upper half plane is in compression, the lower in tension.

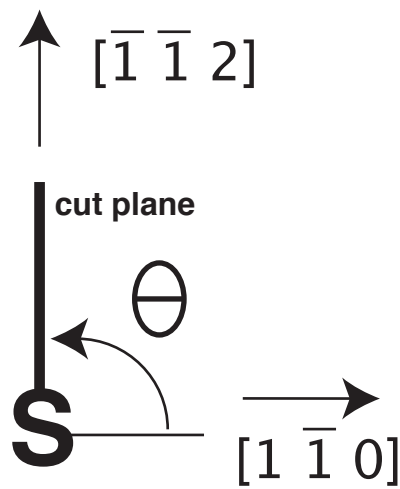


(b) The edge coordinate system

Figure 10: Edge dislocation geometry



(a) Frozen atoms are in blue, free are red. The black line denotes the cut plane; white lines indicate direction for the three partials.



(b) The screw coordinate system. $\langle 1\ 1\ 1 \rangle$ is into the page.

Figure 11: The screw dislocation. The radius of the free region is about 80 Å, and the radius of the entire simulation area is 100 Å. The cylinder is 37.091 Å deep in the periodic direction.

interaction energy will consistently go up the closer the defect is to the core. Atomistics predict the interaction energy rising as the vacancy gets closer, but only until about 6-10 Å from the core. Within this distance, interaction energy becomes negative, indicating a preference to have a vacancy in this part of the tensile region. DTC also predicts no interaction when the defect is on the glide plane, but atomistics disagrees. As far as 20 Å from the core, a negative interaction energy is seen, and less than 10 Å away, the core tends to reorganize to a much lower energy structure, with the vacancy tending to move closer to the core along the glide plane. All results can be seen in Figure 12.

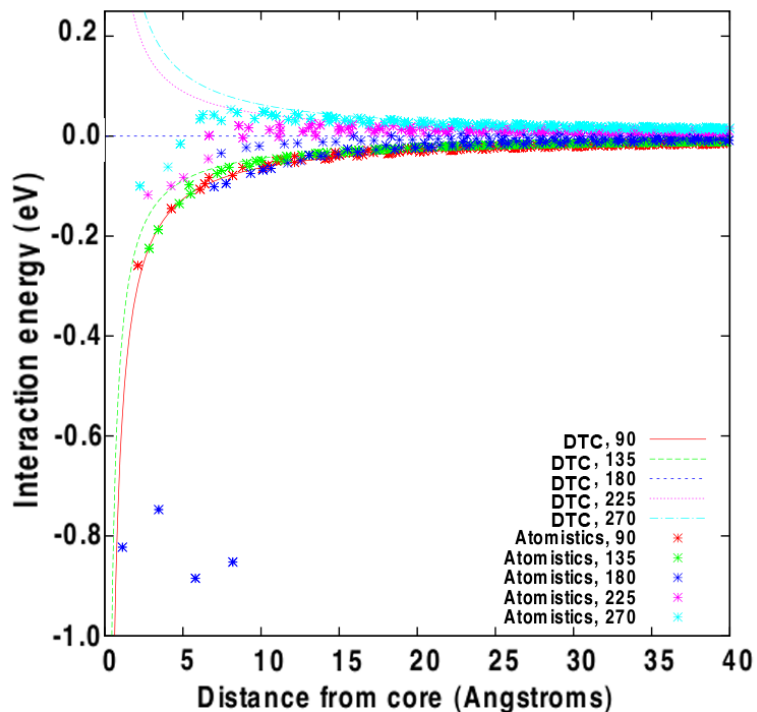
3.4.1.2 Interstitial

A variety of interstitial configurations were tested atomistically. Although in an ideal situation, one can imagine that an interstitial would prefer to be in the tensile half sphere surrounding an edge dislocation, in a realistic damage situation, interstitials will be created in the compressive region as well. Therefore, we have tested dumbbells in both regions.

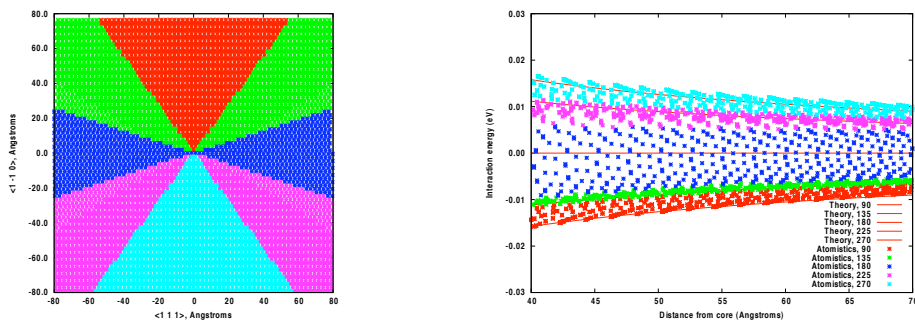
Dumbbells were created along the y -axis in the dislocation coordinate system, the configuration was minimized, and the energy measured. Results for these $[1 \bar{1} 0]$ dumbbells can be seen in Figure 13. In the graph, ‘distance from core’ is defined as the original distance that the center of the created dumbbell was from the core. Some dumbbells tended to rearrange under minimization - these are seen in the figure as points with energy close to -3.0.

Again, far from the core atomistic results agree well with theory. At 90° , the interaction energy is slightly higher than predicted beginning near 25 Å. As we get closer to the core, the predicted interaction energy has a peak at about 7 Å before beginning to slightly fall. The same trend, with opposite signs, is seen for 270° , directly below the extra half plane.

At 180° no interaction is predicted, but there is actually a strong interaction below 10 Å, resulting in climb of the dislocation. All dumbbells created within this distance tended to reorganize the core, giving the same low-energy structure in each case. This close-up of this structure transition can be seen in Figure 14. The upper member of the dumbbell slid down and joined the glide plane, restoring the ‘perfect’ compression. The lower half of the



(a) Atomistics include a wider range of angle than DTC, as shown below.



(b) This shows the atoms included within each angle measurement for the atomistics. Angle is well measured from the positive x-axis. Angles labeled nominally only include the left half plane, however the edge dislocation is symmetric about the y-axis.

(c) Far from the core, DTC and atomistics match

Figure 12: DTC vs atomistics for vacancies near an edge dislocation.

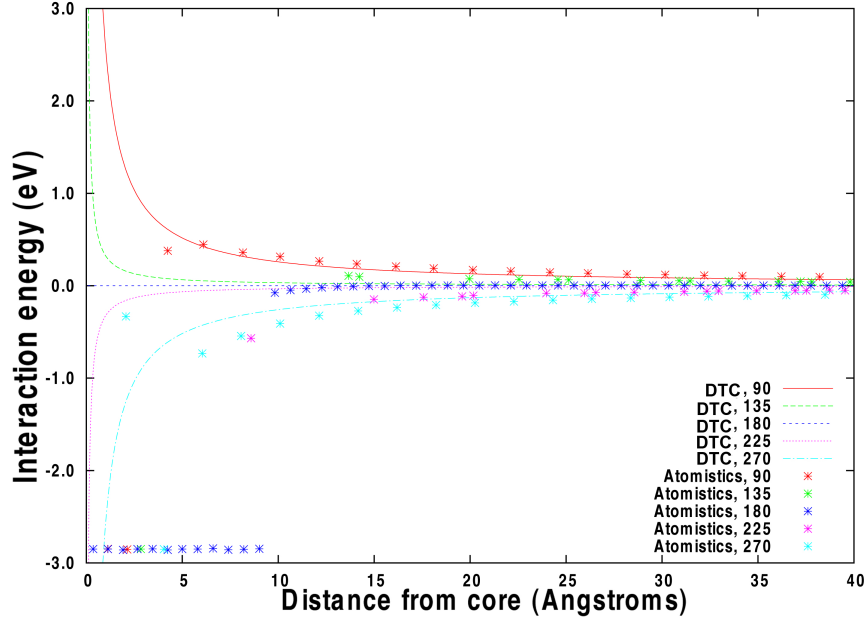


Figure 13: Interaction energies from (initially) $[1 \bar{1} 0]$ dumbbells near an edge dislocation along with DTC calculations.

dumbbell fits into the row of atoms below the glide plane. This generates a crowdion in the $\langle 1 1 1 \rangle$ direction, effectively creating two jogs in the dislocation, $\sqrt{6}a_0/6$ apart, along the direction of the dislocation line. This is illustrated in perspective view in Figure 15. The same behavior is seen for other angles, but only for the atoms closest to the core, within 5 Å or less.

In the dislocation coordinate system, $[1 \bar{1} 0]$ and the equivalent $[\bar{1} 1 0]$ dumbbells have extent in only the y -direction, while $[1 1 0]$ and equivalent $[\bar{1} \bar{1} 0]$ dumbbells have extent

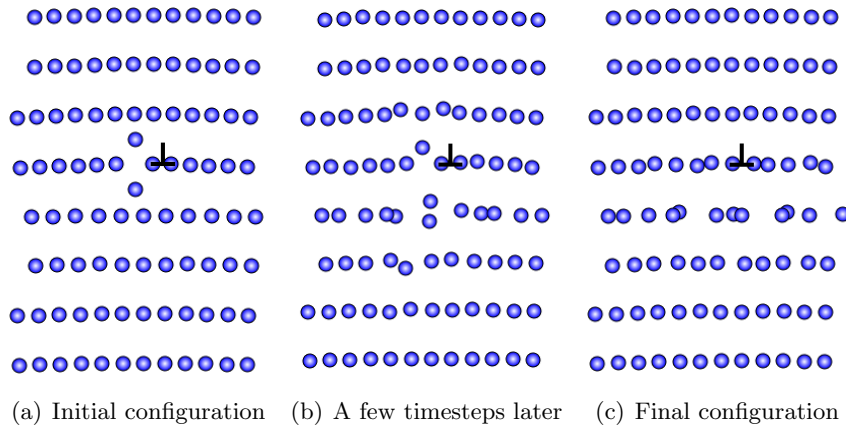


Figure 14: A $[1 \bar{1} 0]$ dumbbell at 180° reorganizes into a jog. The core location is indicated.

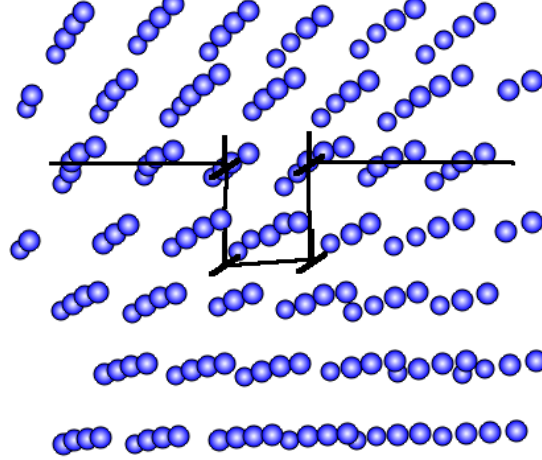


Figure 15: Jogs in an edge dislocation after reorganization of a dumbbell near the core.

in the x and z directions. This could lead to a difference in energy between the two configurations. This was tested at 270° . In fact, there are extremely minimal differences in energy between these two cases, except for very near the core when there are differences in whether or not the dumbbells rearrange into the aforementioned jog configuration. Similar patterns hold true for the other 4 possible $\langle 1\ 1\ 0 \rangle$ orientations. As can be seen in Figure 16, all of the variations are closely spaced in energy, with $\langle 1\ 1\ 0 \rangle$ and $\langle 1\ 0\ 1 \rangle$ orderings lying mostly on top of each other in energy. All of the dumbbells have stronger interactions than predicted by DTC by approximately 0.25 eV near the core, with DTC and atomistics agreeing better at long distances.

The $\langle 1\ 1\ 1 \rangle$ configuration was also tested. This shape is known to be less stable in bulk crystal and has a higher formation energy; these features are replicated well by the chosen potential. The majority of these dumbbells converted to variants of $\langle 1\ 1\ 0 \rangle$ dumbbells under minimization, while the rest would presumably also convert if any dynamics were run.

3.4.2 Screw

3.4.2.1 Vacancy

ϵ^D has no diagonal components and even under transformation to the crystal coordinate system maintains its zero trace. Thus, DTC predicts no interaction of a vacancy with a screw

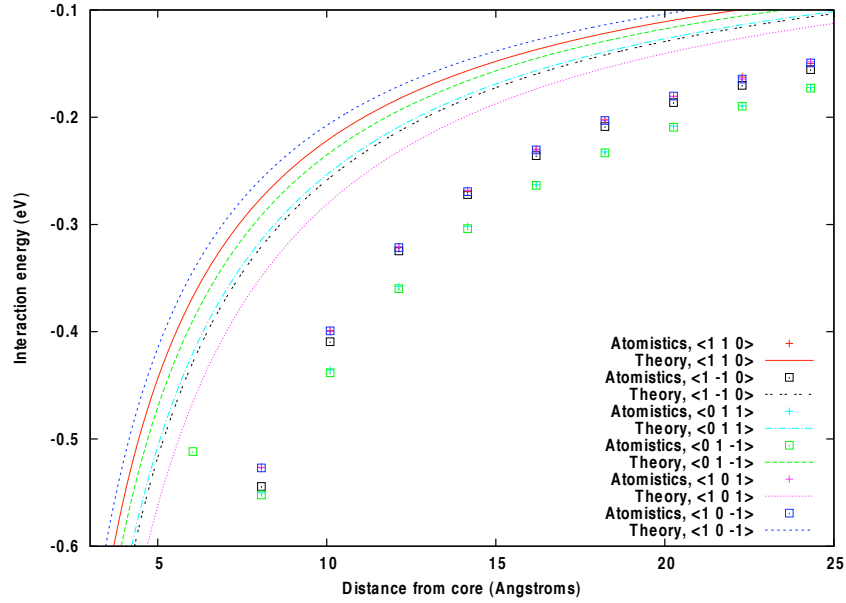
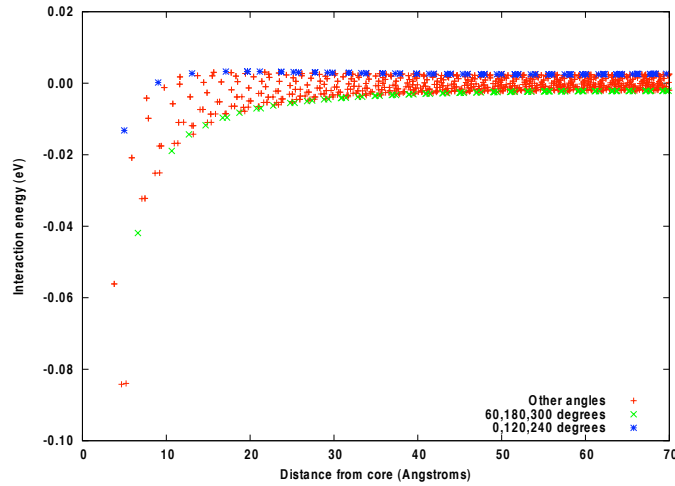


Figure 16: Energies for a variety of $\langle 1\ 1\ 0 \rangle$ dumbbell permutations, compared to DTC, near an edge dislocation. All dumbbells are positioned at 270° .

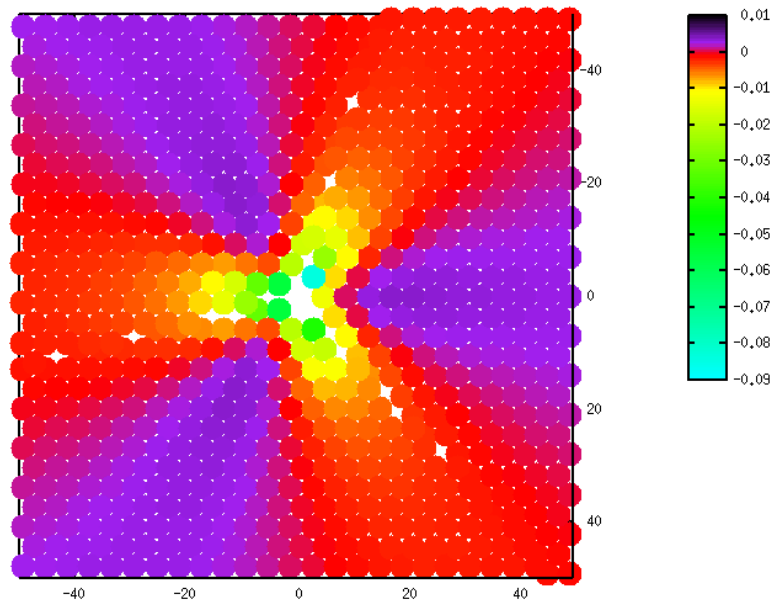
dislocation in an isotropic medium where \mathbf{P} has only diagonal components. Atomistics, however, do show an interaction when the vacancy is close to the core, up to a distance of about $28\ \text{\AA}$ away. To create the graph shown in Figure 17, the same method as for the edge was followed. The variation in energy, larger near the core, is due to the split structure of the core. Slightly positive interaction energies are seen at 0° , 120° , and 240° , or $[1\ \bar{1}\ 0]$, $[\bar{1}\ 0\ 1]$, and $[0\ 1\ \bar{1}]$ respectively. Negative interaction energies are seen at 60° , 180° , and 300° , or $[0\ \bar{1}\ 1]$, $[\bar{1}\ 1\ 0]$, and $[1\ 0\ \bar{1}]$ respectively. Energies for all other angles fall between these two extremes. Very near the core, all interaction energies become negative.

3.4.2.2 Interstitial

Dumbbells of various orientations were inserted around screw cores and the system minimized. First, $[1\ \bar{1}\ 0]$ were considered. At 0° and 180° , dumbbells were pointed directly into the core. The former angle yielded the strongest negative interaction energies, while the latter showed the most positive interaction energies. Positive interaction energies were



(a) Notice the variation in energy with angle, due to the splitting of the core.



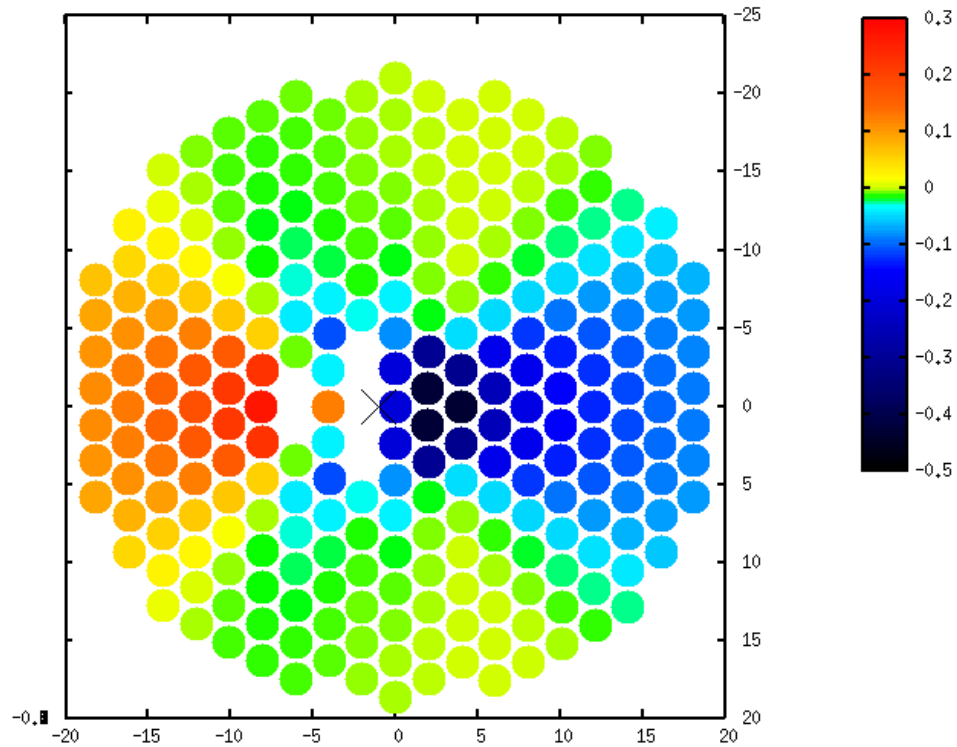
(b) Another perspective on variation of energy with angle. Distances along x and y axes in Å energy in eV.

Figure 17: Interaction energy of vacancies with a screw dislocation as a function of distance from the core and angle. DTC predicts no interaction, but non-negligible interaction is seen up to about 28 Å from the core.

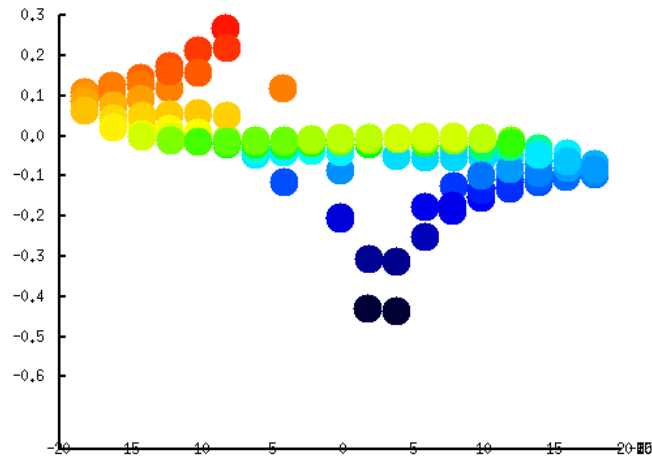
seen for all angles between approximately 140° and 220° ; very slightly positive interaction were also seen near 60° and 300° . Interactions were symmetric about the $[1 \bar{1} 0]$ axis. A color representation of interaction energies can be seen in Figure 18. For comparison, a similar graph from DTC is shown in Figure 19. DTC predicts much stronger energies than atomistics shows near the core (where we would expect linear elastic theory to break down). In addition, the patterns of positive and negative regions are different between DTC and experiment. DTC predicts a clear break between positive and negative energies about the y -axis, however that is not what is seen in atomistics. Although the directions of the strongest positive and negative interactions are consistent, there are differences in strength of the interactions.

Next, $[\bar{1} 1 0]$ dumbbells were tested; this corresponds to a dumbbell lying along $\theta=120^\circ$. A similar pattern was seen, with 120° having the strongest negative interactions and the opposing direction having the strongest positive. This demonstrates that the tri-fold symmetry is still in effect, with dumbbells rotated by 120° showing the same energy patterns. Under minimization, $\langle 1 1 0 \rangle$ dumbbells tended to reorient slightly to fit in with the helical nature of a screw dislocation, but still essentially maintained their character.

Additionally, $[1 1 \bar{2}]$ dumbbells were tested, to see if the same pattern mentioned above could be arbitrarily rotated. This configuration is unstable in most of the locations around the core. Between 0° and 180° , dumbbells reoriented to the $[\bar{1} 0 1]$ direction; between 180° and 360° , they became $[0 1 \bar{1}]$ dumbbells. These are the lowest energy structures within the angles given, due to the tri-fold symmetry. Around 0° , the $[1 \bar{1} 0]$ would actually give the lowest energy, but reaching this orientation would require a rotation of 90° instead of 30° , so no dumbbells acquire this shape under simple minimization. Dumbbells that happened to lie within the most favorable angles (that is, 120° for $[\bar{1} 0 1]$ and 240° for $[0 1 \bar{1}]$) had the strongest negative interaction energies, as would be expected from above evidence. At 180° , all dumbbells maintained their original orientation, unless within 5 \AA of the core. At 0° , all dumbbells farther than 50 \AA from the core are also metastable; dumbbells within this distance sometimes fell to one of the $\langle 1 1 0 \rangle$ variants, depending on the exact θ . Under even more stringent minimization, most of the dumbbells at this angle could be expected to

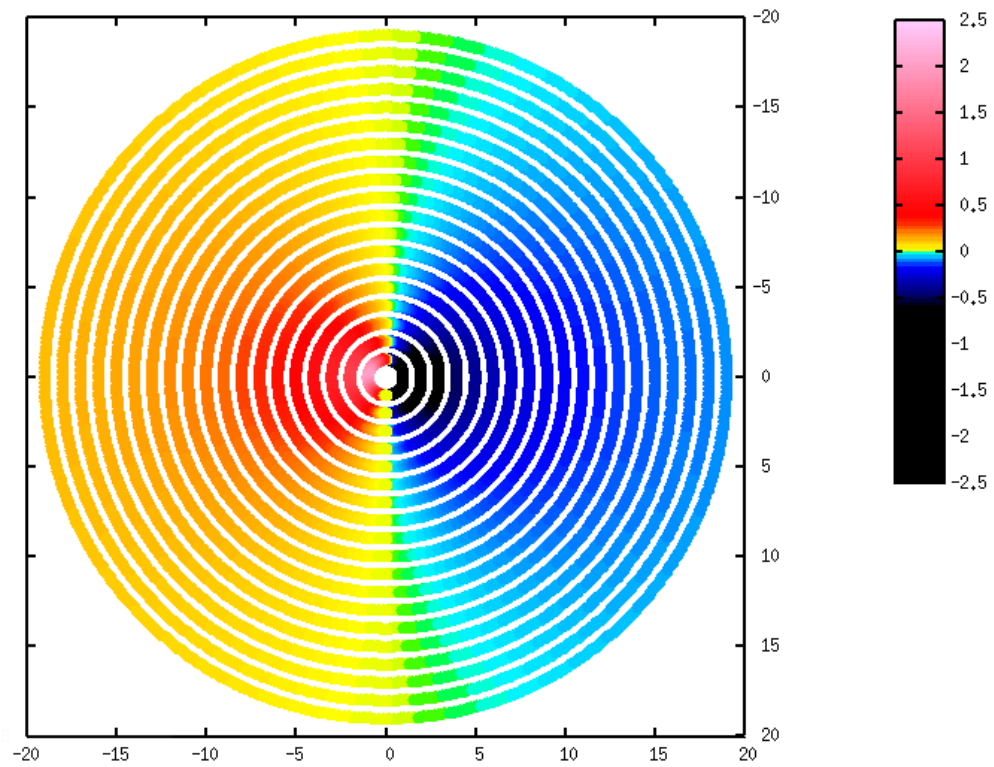


(a) View down the core, which is marked with an X. Orientation of axes is the same as above. Each point denotes a relaxed lattice position in a core without defects, about which a dumbbell was generated. Missing points near the core indicate that the dumbbell was not a stable configuration, and the core reorganized to a lower energy structure that is off-scale.



(b) A view of position along the $\langle 1 \bar{1} 0 \rangle$ axis vs energy. This picture gives an idea of the variation in energy values.

Figure 18: Color representation of interaction energies of (stable) $[1 \bar{1} 0]$ dumbbells with a screw dislocation from atomistics. Distance are in Å energies in eV.



(a) View down the core. Orientation of axes is the same as above.

Figure 19: Color representation of interaction energies of $[1 \bar{1} 0]$ dumbbells with a screw dislocation from theory. Distance are in Å energies in eV. The colors correspond between the above graph and this one.

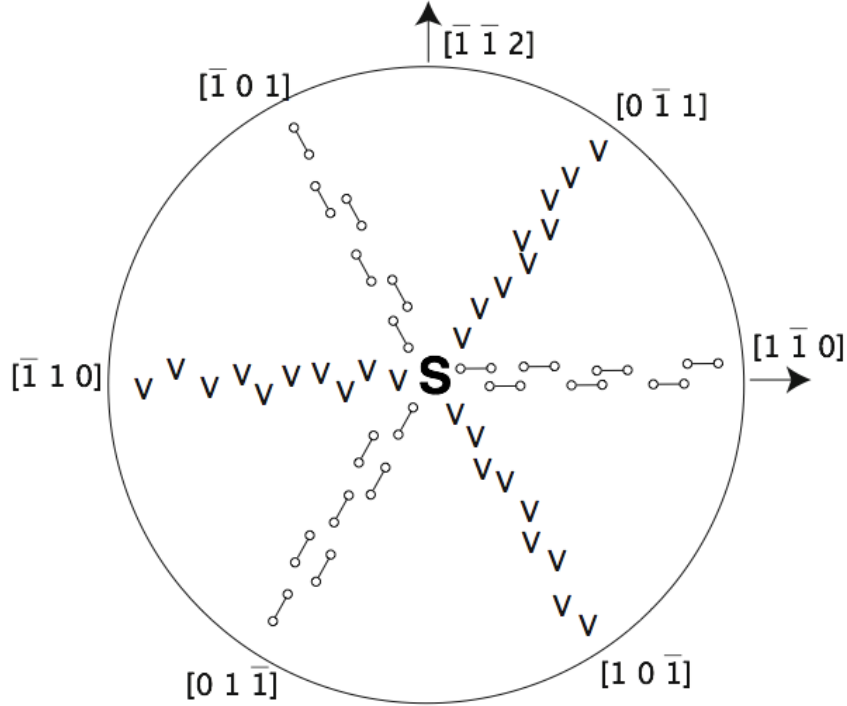


Figure 20: The most favorable orientations and positions for defects around a screw dislocation.

reorient. For dumbbells that kept the $[1\ 1\ \bar{2}]$ shape, the total system energy was about 0.5 eV higher than for the systems that rearranged themselves, confirming that this structure is metastable at best. Due to the reorientation to favorable configurations, only neutral or negative interaction energies were observed.

In summary, dumbbells oriented towards the core on any of the tri-fold splitting directions (0° , 120° , and 240°) have the strongest negative interaction energies; dumbbells across the core from these, and within approximately 40° on either side, have positive interactions. Other orientations that lie within the the plane perpendicular to ξ will reorient to one of the low energy structures. Figure 20 shows the most energetically favorable positions and orientations for interstitial dumbbells and vacancies around the dislocation. Since it is energetically favorable for vacancies and SIAs to lie in different regions around the core, recombination may be slowed down and higher numbers of defects that would be expected from continuum theory may exist.

3.5 Discussion

Dipole tensors have been calculated for a number of different point defect orientations. These allow for prediction of interaction energies between dislocations and defects according to continuum elasticity theory. Because this theory breaks down near the core of a dislocation, comparison with atomistics is needed for accurate modeling of irradiation creep in structural materials. Significant differences were found between DTC and atomistics for many important configurations.

In the edge dislocation, $\langle 1\ 1\ 0 \rangle$ dumbbells were found to be the most stable configuration in many locations around the core. However, under minimization some reorganized to create a double jog, resulting in climb. This phenomenon was most prevalent on the glide plane. $\langle 1\ 1\ 1 \rangle$ dumbbells were also investigated, but most converted to $\langle 1\ 1\ 0 \rangle$ shapes, even in the 0 K test environment. Vacancies also interacted more strongly than would be expected according to DTC, including having negative interaction energies in the expansive region below the glide plane, when within about 10 Å from the core. Vacancies on the glide plane were absorbed by the core more readily than vacancies lying at other angles.

The atomistics were able to reveal the true split nature of the bcc screw dislocation, a feature not predicted by the elastic strain field of equation 3. Vacancies do have a weak, but non-negligible, interaction with the dislocation; DTC predicts none at all. This interaction is dependent on the positioning of the vacancy due to the core splitting. Self-interstitial dumbbell interactions also strongly depend on the angle and orientation about the core; dumbbells on the plane perpendicular to the dislocation line have three stable configurations, pointed in towards the core at 0, 120, and 240°. For a particular orientation, the energy profile with angle varies between negative and positive twice, when further than about 8 Å from the core (energies are mostly negative within this distance). However, DTC only predicts a single change from negative to positive at 90°; also the interactions are predicted to be much stronger at many angles. Due to the different preferred positions of vacancies and interstitials around the core, recombination may be impeded; this effect is ignored in continuum theory.

For both types of dislocation, atomistics shows a negative interaction energy very near

the core at all angles. DTC often shows a positive interaction energy for some angles all the way up to the core.

Overall, continuum theory and DTC explain some features of interactions between dislocation and point defects but fail in many respects when compared to atomistics. Future work needs to be done to determine how influential these differences are in macroscopic creep calculations and the implications for reactor structural component lifetimes.

CHAPTER IV

CONCLUSIONS

Two studies of irradiation damage in iron have been presented. First, damage cascade molecular dynamics simulations were performed in pure iron and iron with hydrogen interstitials at a variety of PKA energies. It was found that the percentage of defects that survive relaxation is approximately 1.25%, averaging over all systems. No significant difference was found in the character of the primary damage state between systems with and without hydrogen. This does not necessarily mean that the long term behavior of these two systems will be the same, however.

Second, interaction energies between point defects and edge and screw dislocations were calculated with atomistic simulations and with a dipole tensor and continuum theory based method. It was shown that dipole tensor calculations miss important information that atomistic calculation reveal, particularly relevant to the screw core structure. Linear elastic theory breaks down near the core of either type of dislocation, so atomistic simulations are a valuable tool in this region. Evidence for climb and creep was seen in the case of the edge dislocation.

In conclusion, atomistics can be a valuable tool for analysis of defect structures. Understanding both the processes that create defects and how defects interact after creation is necessary to predict macroscopic behavior of materials in irradiated environments.

APPENDIX A

MANY-BODY EAM AND FS POTENTIALS

Choosing an appropriate potential is essential for obtaining quality results in any atomistic calculation. The traditional formalism of a pair potential, such as a Lennard-Jones or Morse potential, assumes that the total energy of the solid, E_{coh} , can be expressed as a sum over all of the individual pair bonds. However, this is just an assumption, one that turns out to be impossible to prove theoretically.

In reality, a many-body potential is needed to account for the influence that bonds between atoms have on each other. To deal with this, the embedded-atom method (EAM) was developed by Daw and Baskes in 1983 [12, 13, 14] for metallic solids. Essentially, each atom is treated as if it were a defect embedded in an electron gas created by the presence of all the other atoms. The cohesive energy of the system can be described in two parts by an embedding energy and an electrostatic interaction with a sum over all atoms in the system:

$$E_{coh} = \sum_i G_i \left(\sum_{j \neq i} \rho_j^a(R_{ij}) \right) + \frac{1}{2} \sum_{i,j(j \neq i)} \phi_{ij}(R_{ij})$$

where G is the embedding energy, ρ^a is the spherically averaged atomic electron density, R_{ij} is the distance between atoms i and j , and ϕ is an electrostatic, two-atom interaction. With this formulation, atoms that are near defects or surfaces, for example, will feel a different density profile than atoms in the bulk, allowing the potential to treat significantly more complex systems than pair potentials alone.

While more complex systems can be treated, implementing the method is no more difficult than implementing a pair potential. The functions $G(\rho)$ and $\phi(R)$ can be found either from first principles or using semi-empirical methods. Normally, they are fit to data from a particular (pure) metal, such as lattice constants, elastic constants, or defect formation energies.

A similar method was developed simultaneously by Finnis and Sinclair (FS) [18]. For pure metals, the two methods are exactly equivalent. For alloys, the FS ansatz requires different functionals ρ for interactions between different elements, while EAM uses an averaged one.

REFERENCES

- [1] ACKLAND, G., BACON, D., CALDER, A., and HARRY, T., “Computer simulation of point defect properties in dilute Fe-Cu alloy using a many-body interatomic potential,” *Phil. Mag. A*, vol. 75, no. 3, pp. 713–732, 1997.
- [2] ACKLAND, G., MENDELEV, M., SROLOVITZ, D., HAN, S., and BARASHEV, A., “Development of an interatomic potential for phosphorus impurities in alpha-iron,” *J. Phys.: Condens. Matter*, vol. 16, pp. S2629–S2642, 2004.
- [3] BACON, D., GAO, F., and OSETSKY, Y., “The primary damage state in fcc, bcc and hcp metals as seen in molecular dynamics simulations,” Jan 2000.
- [4] BACON, D., OSETSKY, Y. N., and RONG, Z., “Computer simulation of reactions between an edge dislocation and glissile self-interstitial clusters in iron,” *Philos Mag*, vol. 86, pp. 3921–3936, Jan 2006.
- [5] BEHRISCH, R., “Measurement of hydrogen isotopes in plasma-facing materials of fusion devices,” *Physica Scripta*, vol. T94, pp. 52–57, 2001.
- [6] BULLOUGH, R. and HAYNS, M., “Irradiation-creep due to point-defect absorption,” *Journal of Nuclear Materials*, vol. 57, no. 3, pp. 348–352, 1975.
- [7] BULLOUGH, R. and WILLIS, J., “Stress-induced point defect-dislocation interaction and its relevance to irradiation creep,” *Philosophical Magazine*, vol. 31, no. 4, pp. 855–861, 1975.
- [8] BULLOUGH, R. and WOOD, M., “Mechanisms of radiation-induced creep and growth,” *Journal of Nuclear Materials*, vol. 90, pp. 1–21, Jan 1980.
- [9] CALDER, A. and BACON, D., “A molecular-dynamics study of displacement cascades in alpha-iron,” *Journal of Nuclear Materials*, vol. 207, pp. 25–45, Jan 1993.
- [10] CATURLA, M., SONEDA, N., ALONSO, E., WIRTH, B., DE LA RUBIA, T., and PERLADO, J., “Comparative study of radiation damage accumulation in Cu and Fe,” Jan 2000.
- [11] CHRISTIAN, J. and VITEK, V., “Dislocations and stacking faults,” *Reports on Progress in Physics*, vol. 33, pp. 307–411, 1970.
- [12] DAW, M. and BASKES, M., “Semiempirical, quantum-mechanical calculation of hydrogen embrittlement in metals,” *Phys Rev Lett*, vol. 50, pp. 1285–1288, Jan 1983.
- [13] DAW, M. and BASKES, M., “Embedded-atom method - derivation and application to impurities, surfaces, and other defects in metals,” *Physical Review B*, vol. 29, pp. 6443–6453, Jan 1984.
- [14] DAW, M., FOILES, S., and BASKES, M., “The embedded-atom method - a review of theory and applications,” *Mater Sci Rep*, vol. 9, pp. 251–310, Jan 1993.

- [15] DEDERICHS, P. H. and SCHROEDER, K., "Anisotropic diffusion in stress fields," *Phys. Rev. B*, vol. 17, pp. 2524–2536, Mar 1978.
- [16] DOMAIN, C. and MONNET, G., "Simulation of screw dislocation motion in iron by molecular dynamics simulations," *Phys Rev Lett*, vol. 95, p. 215506, Nov 2005.
- [17] DUESBERY, M., VITEK, V., and BOWEN, D., "Effect of shear-stress on screw dislocation core structure in body-centered cubic lattices," *P Roy Soc Lond A Mat*, vol. 332, pp. 85–111, Jan 1973.
- [18] FINNIS, M. and SINCLAIR, J., "A simple empirical n-body potential for transition metals," *Philosophical magazine. A. Physics of condensed matter. Defects and mechanical properties*, vol. 50, no. 1, pp. 45–55, 1984.
- [19] FREDERIKSEN, S. and JACOBSEN, K., "Density functional theory studies of screw dislocation core structures in bcc metals," *Philos Mag*, vol. 83, pp. 365–375, Jan 2003.
- [20] FUJITA, S., OKITA, T., KURAMOTO, E., and SEKIMURA, N., "A study of the interaction between irradiation induced-defect and a line dislocation in bcc-iron," *Journal of Nuclear Materials*, vol. 386-388, pp. 93–96, Feb 2009.
- [21] GRANDE, N. S.-D., SAVINO, E., and C.N.TOME, "Stress induced anisotropic diffusion of intrinsic point defects towards dislocations in h.c.p. crystals," *Phys. Stat. Sol. (b)*, vol. 144, p. 271, 1987.
- [22] HAFTEL, M., ANDREADIS, T., LILL, J., and ERIDON, J., "Surface relaxation of alpha-iron and the embedded-atom method," *Physical Review B*, vol. 42, pp. 11540–11552, Jan 1990.
- [23] HARRISON, R., VOTER, A., and CHEN, S., "Embedded atom potential for bcc iron," *Atomistic Simulation of Materials - Beyond Pair Potentials*, pp. 219–222, 1989.
- [24] HEALD, P. and SPEIGHT, M., "Steady-state irradiation creep," *Philosophical Magazine*, vol. 29, no. 5, pp. 1075–1080, 1974.
- [25] HENKELMAN, G., UBERUAGA, B., and JONSSON, H., "A climbing image nudged elastic band method for finding saddle points and minimum energy paths," *J Chem Phys*, vol. 113, pp. 9901–9904, Jan 2000.
- [26] HESKETH, R. *Philosophical Magazine*, vol. 8, no. 7, pp. 1417–20, 1962.
- [27] HIRTH, J. and LOTHE, J., *Theory of Dislocations*. John Wiley and Sons, Inc., 2nd ed., 1982.
- [28] JIANG, D. and CARTER, E. A., "Diffusion of interstitial hydrogen into and through bcc Fe from first principles," *Physical Review B*, vol. 70, no. 6, p. 64102, 2004.
- [29] JOHNSON, R. and OH, D., "Analytic embedded atom method model for bcc metals," *J Mater Res*, vol. 4, pp. 1195–1201, Jan 1989.
- [30] KANZAKI, H., "Point defects in face-centered cubic lattice - I : Distortion around defects," *J. Phys. Chem. Solids*, vol. 2, pp. 24–36, 1957.

- [31] LIU, X. and BINER, S., “Molecular dynamics simulations of the interactions between screw dislocations and self-interstitial clusters in body-centered cubic Fe,” *Scripta Materialia*, vol. 59, no. 1, pp. 51–54, 2008.
- [32] MALERBA, L., “Molecular dynamics simulation of displacement cascades in α -Fe: a critical review,” *Journal of Nuclear Materials*, vol. 351, no. 1-3, pp. 28–38, 2006.
- [33] MATTHEWS, J. and FINNIS, M., “Irradiation creep models - an overview,” *J. Nuc. Mat.*, vol. 159, pp. 257–285, 1988.
- [34] MEISSNER, N., SAVINO, E., WILLIS, J., and BULLOUGH, R., “The dislocation loop in an anisotropic medium and its interaction with an interstitial atom,” *Phys. Stat. Sol. (b)*, vol. 63, pp. 139–151, 1974.
- [35] MENDELEV, M., HAN, S., SROLOVITZ, D., ACKLAND, G., SUN, D., and ASTA, M., “Development of new interatomic potentials appropriate for crystalline and liquid iron,” *Phil. Mag.*, vol. 83, no. 35, pp. 3977–3994, 2003.
- [36] MONTI, A., SARCE, A., GRANDE, N. S.-D., SAVINO, E., and TOME, C., “Point-defects and sink strength in hcp metals,” Jan 1991.
- [37] MORIARTY, J., VITEK, V., BULATOV, V., and YIP, S., “Atomistic simulations of dislocations and defects,” Jan 2002.
- [38] NABARRO, F. R. N., *Theory of Crystal Dislocations*. Clarendon Press, Oxford, 1967.
- [39] OSETSKY, Y. N., BACON, D., SERRA, A., and SINGH, B. N., “Interactions between edge dislocations and interstitial clusters in iron and copper,” *Mat.Res.Soc.Symp.Proc.*, vol. 653, pp. Z3.4.2–Z3.4.6, Jun 2001.
- [40] PLIMPTON, S., “Fast parallel algorithms for short-range molecular dynamics,” *J. Comp. Phys.*, vol. 117, pp. 1–19, 1995. <http://lammps.sandia.gov>.
- [41] RAMASUBRAMANIAM, A., ITAKURA, M., and CARTER, E. A., “Interatomic potentials for hydrogen in alpha-iron based on density functional theory,” *Phys. Rev. B*, vol. 79, no. 17, p. 174101, 2009.
- [42] SAN-MARTIN, A., MANCHESTER, F. D., and EDITED BY H. OKAMOTO, *Phase Diagrams of Binary Iron Alloys*. ASM International, 1993.
- [43] SAVINO, E. and TOMÉ, C., “Irradiation creep by stress-induced preferential attraction due to anisotropic diffusion (SIPA-AD),” *J. Nuc. Mat.*, vol. 108 & 109, pp. 405–416, 1982.
- [44] SCHAUBLIN, R. and BALUC, N., “Radiation damage in ferritic/martensitic steels for fusion reactors: a simulation,” *Nucl. Fusion*, vol. 47, pp. 1690–1695, 2007.
- [45] SHASTRY, V. and DE LA RUBIA, T., “The interaction between point defects and edge dislocation in bcc iron,” *Journal of Engineering Materials and Technology*, vol. 121, p. 126, 1999.
- [46] SIMONELLI, G., PASIANOT, R., and SAVINO, E., “Point-defect computer-simulation including angular forces in bcc iron,” *Physical Review B*, vol. 50, pp. 727–738, Jan 1994.

- [47] SIVAK, A. B., CHERNOV, V. M., DUBASOVA, N. A., and ROMANOV, V. A., “Anisotropy migration of self-point defects in dislocation stress fields in bcc Fe and fcc Cu,” Jan 2007.
- [48] SØRENSEN, M. and VOTER, A., “Temperature-accelerated dynamics for simulation of infrequent events,” *The Journal of Chemical Physics*, vol. 112, p. 9599, 2000.
- [49] STOLLER, R., “Primary damage formation in irradiated materials,” *JOM(USA)*, vol. 48, no. 12, pp. 23–27, 1996.
- [50] STOLLER, R., ODETTE, G., and WIRTH, B., “Primary damage formation in bcc iron,” *Journal of Nuclear Materials*, vol. 251, pp. 49–60, 1997.
- [51] TERYTYEV, D., LAGERSTEDT, C., OLSSON, P., NORDLUND, K., WALLENUS, J., BECQUART, C., and MALERBA, L., “Effect of the interatomic potential on the features of displacement cascades in alpha-fe: A molecular dynamics study,” Jan 2006.
- [52] TOME, C., CECATTO, H., and SAVINO, E., “Point-defect diffusion in a strained crystal,” *Physical Review B*, vol. 25, no. 12, pp. 7428–7440, 1982.
- [53] TOME, C. and SAVINO, E., “Interaction between point-defects and straight dislocations in hexagonal crystals,” *Mater Sci Eng*, vol. 24, pp. 109–122, Jan 1976.
- [54] VITEK, V., “Computer-simulation of screw dislocation-motion in bcc metals under effect of external shear and uniaxial stresses,” *P Roy Soc Lond A Mat*, vol. 352, pp. 109–124, Jan 1976.
- [55] VITEK, V., “Structure of dislocation cores in metallic materials and its impact on their plastic behavior,” *Prog Mater Sci*, vol. 36, pp. 1–27, Jan 1992.
- [56] VITEK, V., “Core structure of screw dislocations in body-centred cubic metals: relation to symmetry and interatomic bonding,” *Philos Mag*, vol. 84, pp. 415–428, Jan 2004.
- [57] WAS, G. S., *Fundamentals of Radiation Materials Science: Metals and Alloys*. Springer, 2007.
- [58] YANG, L., ZU, X., XIAO, H., GAO, F., HEINISCH, H., KURTZ, R., and LIU, K., “Atomistic simulation of helium-defect interaction in alpha-iron,” *Applied Physics Letters*, vol. 88, p. 091915, 2006.
- [59] YU, J., YU, G., YAO, Z., and SCHAUBLIN, R., “Synergistic effects of PKA and helium on primary damage formation in Fe–0.1% He,” *Journal of Nuclear Materials*, vol. 367, pp. 462–467, 2007.